





Wavelet analysis of the coupling between turbulence, particles and electrostatics in dust storms

Huan Zhang¹  and Xiaojing Zheng² 

¹Center for Particle-laden Turbulence, Lanzhou University, Lanzhou 730000, PR China

²Research Center for Applied Mechanics, Xidian University, Xi'an 710071, PR China

Corresponding author: Xiaojing Zheng, xjzheng@lzu.edu.cn

(Received 21 May 2024; revised 18 December 2024; accepted 18 January 2025)

Dust storms are a unique form of high-Reynolds-number particle-laden turbulence associated with intense electrical activity. Using a wavelet-based analysis method on field measurement data, Zhang *et al.* (2023 *J. Fluid Mech.* **963**, A15) found that wind velocity intermittency intensifies during dust storms, but it is weaker than both dust concentration and electric field. However, the linear and nonlinear multifield coupling characteristics, which significantly influence particle transport and turbulence modulation, remain poorly understood. To address this issue, we obtained high-fidelity datasets of wind velocity, dust concentration, and electric field at the Qingtu Lake Observation Array. By extending the wavelet-based data analysis method, we investigated localised linear and quadratic nonlinear coupling characteristics in strong turbulence–particle–electrostatics coupling regimes. Our findings reveal that linear coupling behaviour is largely dominated by the multifield intermittent components. At small scales, due to very high intermittency, no strong phase synchronisation can be formed, and the interphase linear coupling is weak and notably intermittent. At larger scales, however, perfect phase synchronisation emerges, and dust concentration and electric field exhibit strong, non-intermittent linear coupling, suggesting that large-scale coherent structures play a dominant role in driving the coupling. Importantly, the multifield spectra show well-developed -1 and $-5/3$ power-law regions, but the spectral breakpoints for dust concentration and electric field are two decades lower than that for streamwise wind velocity. This difference is due to the broader range and stronger intensity of quadratic nonlinear coupling in dust concentration and electric field, which leads to the broadening of Kolmogorov's $-5/3$ power-law spectrum.

Key words: atmospheric flows, particle/fluid flows, intermittency

1. Introduction

Dust storms pose a unique opportunity to study particle-laden turbulent flows at extremely high-Reynolds numbers. Several physical mechanisms, including cleavage/fractoelectrification, bombardment charging, pyroelectrification, piezoelectrification, polarisation by Earth's atmospheric electric field, triboelectrification and contact electrification (Kanagy & Mann 1994; Zheng 2013), are believed to cause dust particles to acquire a substantial charge, thereby generating electric fields with intensities exceeding 100 kV m^{-1} (e.g. Rudge 1913; Stow 1969; Schmidt, Schmidt & Dent 1998; Shinbrot & Herrmann 2008; Williams *et al.* 2009; Zhang & Zhou 2020; Rahman, Cheng & Samtaney 2021). Consequently, in addition to the particle–turbulence couplings in ordinary particle-laden turbulent flows, particle–electrostatics couplings also play a crucial role (e.g. Zheng, Huang & Zhou 2003; Lu *et al.* 2010; Karnik & Shrimpton 2012; Zheng 2013; Grosshans & Papalexandris 2017; Zhang, Cui & Zheng 2023).

Depending on the flow characteristic parameters, turbulence–particle–electrostatics couplings can be categorised into several regimes. Concerning turbulence–particle couplings, when the particle mass loading is low, the influence of particles on turbulence can be disregarded, which is referred to as a one-way coupling regime. When the particle mass loading is high and the volume fraction is small, turbulence is significantly affected by particles, which is referred to as a two-way coupling regime. When both the mass loading and volume fraction of particles are high enough, particle collisions occur, forming a four-way coupling regime (Elghobashi 1994; Balachandar & Eaton 2010; Brandt & Coletti 2022). Regarding particle–electrostatics couplings, when the electrostatic Stokes number of particles is small (or large), particle dynamics is dominated by the inertial (or electrostatic) effects of particles (Grosshans *et al.* 2021; Boutsikakis, Fede & Simonin 2022; Zhang *et al.* 2023). In dust storms, the dust concentration decreases exponentially with height (McGowan & Clark 2008; Zheng 2009). As a result, the mass loading of particles is low at locations far from the wall, allowing the turbulence modulation by particles to be neglected. In contrast, close to the wall, both the mass loading and electrostatic Stokes number of particles are large, indicating a strong turbulence–particle–electrostatics coupling (Zhang & Zhou 2023), which warrants special attention. It is widely recognised that such strong multifield couplings have pronounced effects on particle transport and aggregation (Lu *et al.* 2010; Karnik & Shrimpton 2012; Lu & Shaw 2015; Boutsikakis *et al.* 2022; Zhang *et al.* 2023; Ruan, Gorman & Ni 2024), turbulence modulation (Cui, Zhang & Zheng 2024), the charging properties of particles (Grosshans & Papalexandris 2017; Jantač & Grosshans 2024) and the formation of turbulent electric fields (Di Renzo & Urzay 2018).

One of the major characteristics of dust storms is the significant small-scale intermittency in multiple fields, including wind velocity, the mass concentration of dust particles smaller than $10 \text{ }\mu\text{m}$ (hereafter, PM10 dust concentration) and electric field (Zhang, Tan & Zheng 2023). Intuitively, the time series of these fields displays intense sporadic local fluctuations. Statistically, the probability density function of the increments in these fields deviates increasingly from the Gaussian distribution as the scale decreases (i.e. the flatness increases and exceeds three with decreasing scale), and the high-order structure functions deviate from Kolmogorov linear scaling. Compared to clean-air conditions, the intermittency of wind velocity in dust storms is significantly enhanced at small scales, while it remains largely unchanged at large scales. This may be due to high concentrations of dust particles injecting velocity fluctuations at small scales in the near-surface region (Horwitz & Mani 2020). Notably, at 5 m above the surface, the intermittency of PM10 dust concentration is the strongest in dust storms, followed by the electric field, with wind velocity showing the least intermittency. In short,

compared with the traditional Fourier transform, the wavelet analysis is more suitable for analysing multifield data series recorded in dust storms. This is because the Fourier transform analyses the entire time series globally and provides characteristics in a time-averaged sense, while the wavelet transform provides both time and frequency information (e.g. Meneveau 1991; Daubechies 1992; Farge 1992; Camussi & Guj 1997; Torrence & Compo 1998; Zhou 2021), effectively extracting and characterising intermittent events.

Previous studies have focused on utilising cospectral analysis to investigate the time-averaged linear coupling behaviour in dust storms. For instance, Wang, Zheng & Tao (2017) performed cospectral analysis between the PM10 dust concentration and wind velocity during dust storms. Their findings indicated that low-speed very large-scale motions (VLSMs) reduce the upward flux of PM10 in the logarithmic layer, while high-speed VLSMs enhance the downstream and upward transport of PM10 in higher regions. Subsequently, Zhang & Liu (2023) examined the influence of electric fields on dust transport in dust storms using the cospectrum between PM10 dust concentration and electric field. The results demonstrated that electric fields significantly promote PM10 transport at the kilometer-sized synoptic scale, have a secondary inhibitory effect at the hectometer-sized VLSM scale, and exhibit negligible effects at the decameter-sized turbulent integral scale. Similarly, in wind-tunnel blowing snow experiments, Paterna, Crivelli & Lehning (2016) analysed the cospectrum between measured wind velocity and particle mass flux to explore the effects of turbulence on snow particle entrainment. They identified two regimes of snow particle saltation: (a) a turbulence-dependent regime, where turbulence directly regulates weak saltation; (b) a turbulence-independent regime, where strong saltation develops its own length scale independent of turbulence forcing. Besides linear coupling, various phenomena such as the transition to turbulence, transitions from one turbulence regime to another (Monsalve *et al.* 2020) and energy transfer between different spectral components (Ritz & Powers 1986) can be explained only by the nonlinearity of turbulent flows. Bispectral analysis, as introduced by Hasselmann, Munk & MacDonald (1963) is an effective method to evaluate quadratic phase coupling in the frequency triad f_1 , f_2 and $f_1 + f_2$. Note that quadratic phase coupling is also referred to as three-wave coupling or triadic interactions in the literature (see e.g. Agnon & Sheremet 1997; Xu *et al.* 2003; Biferale, Musacchio & Toschi 2012; Monsalve *et al.* 2020). Strong quadratic coupling processes have been shown to be responsible for spectral energy redistribution (e.g. Elgar & Guza 1985; Ritz & Powers 1986; Dudok de Wit & Krasnosel'skikh 1995), leading to a smoother (Bountin, Shplyuk & Maslov 2008) or broader (Unnikrishnan & Gaitonde 2020) power spectral density (PSD). Despite its paramount importance, bispectral characteristics in dust storms, especially for PM10 concentration and electric field, have not been explored previously.

In the aforementioned time-averaged coupling analysis, an implicit assumption is that coupling behaviour remains uniform over time. However, owing to the intrinsic intermittency of the various interacting fields in dust storms, it is reasonable to anticipate that both linear and quadratic nonlinear couplings exhibit intermittent behaviour across both temporal and scale domains. In particular, coherent structures, which are highly localised in time and scale (Camussi & Guj 1997; Camussi *et al.* 2010), give rise to short-lived, sporadic coupling between turbulent fields (Camussi, Robert & Jacob 2008; Bernardini *et al.* 2023) and are known to contribute significantly to the transport of heat, mass, and momentum (Marusic *et al.* 2010). In this regard, while time-averaged coupling analysis has provided valuable insights into certain multifield interactions in dust storms, this framework is inherently limited in its capacity to capture the critical intermittent coupling dynamics that play a crucial role in these processes.

To elucidate the localised linear and nonlinear coupling characteristics of multiple fields in dust storms, we conducted a series of simultaneous measurements of three-dimensional wind velocity, PM10 dust concentration and electric field at a height of 0.9 m above the surface at the Qingtu Lake Observation Array in 2021. At this measurement height, the particle-to-air mass loading ratio and particle electrostatic Stokes number reached the order of 0.1, indicating significant particle–turbulence and particle–electrostatics couplings. Instead of using a Fourier-based data analysis framework, we adopt a wavelet conditional averaging method based on the local intermittency measure, supplemented by wavelet coherence and bicoherence analyses, to evaluate the multifield localised linear and quadratic nonlinear coupling behaviours.

The remainder of this article is organised as follows: In § 2, we provide detailed information on the 2021 field measurement set-up and the selected high-fidelity dataset. In § 3, we describe the wavelet-based multiple field coupling analysis methods used in this study. The local intermittency, linear coupling and quadratic nonlinear coupling behaviours of multiple fields in dust storms are examined and discussed in detail in §§ 4.1–4.4, respectively. Finally, we summarise the main conclusions of this article in § 5.

2. Dataset

2.1. Measurement set-up

Field measurements were conducted from April to June 2021 at the Qingtu Lake Observation Array (QLOA), an atmospheric surface layer turbulence observatory situated between the Badain Jaran Desert and Tengger Desert in China. The dry lake bed of Qingtu Lake, which spans a flat surface covering approximately 20 km², is devoid of roughness elements such as rocks, vegetation and sand dunes. This extensive flat surface ensures that the atmospheric surface-layer flows at the QLOA site can be considered analogous to the canonical turbulent boundary layers over flat plates after performing standard data quality control procedures (see below) (Hutchins & Marusic 2007; Hutchins *et al.* 2012). From April to June, the QLOA site experiences frequent dust storms due to Mongolian cyclones accompanied by strong northwesterly surface winds (Zheng 2009), offering an excellent opportunity to study randomly occurring dust storms.

The three-dimensional wind velocity components, denoted by U , V and W for the streamwise, spanwise and wall-normal directions respectively, along with the ambient temperature (θ), were measured at heights of $z = \{0.5, 0.9, 1.5, 2.5, 3.49, 5, 7.15, 10.24, 14.65, 20.96, 30\}$ m above the surface. Simultaneously, the PM10 dust concentration (C) and electric field (E) were recorded at a height of 0.9 m. Additionally, the size distribution of total airborne dust particles was determined by analysing the particle sample collected at 0.9 m height (Microtrac S3500 tri-laser particle size analyzer, Verder Scientific). At this measurement height, the total particle concentration is sufficiently high to bring about strong turbulence–particle–electrostatics couplings, yet it avoids reaching excessively high particle concentrations that could cause the measurement instruments to cease functioning. Throughout this article, the fluctuating components of the measured physical quantities are represented by lowercase letters u , v , w , θ , c and e . The wind velocities and ambient temperatures were recorded using sonic anemometers (CSAT3B, Campbell Scientific), PM10 dust concentration was measured using a DustTrak II Aerosol Monitor (Model 8530EP, TSI Incorporated), and the electric field was monitored using an electric field mill (CS110, Campbell Scientific). In addition to the size distribution of total airborne dust particles, all other physical quantities were

monitored in real-time. The sampling frequency of CSAT3B is 50 Hz, while that of 8530EP and CS110 is 1 Hz. All instruments were factory calibrated to meet the following specifications: the offset error of the CSAT3B was less than $\pm 8 \text{ cm s}^{-1}$; the zero drift of the 8530EP was within $\pm 0.002 \text{ kg m}^{-3}$ over 24 hours; and the accuracy of the CS110 was $\pm 5 \%$ of the reading, with a maximum offset of 8 V m^{-1} .

2.2. Dataset description

Since atmospheric flows are uncontrolled, we need to perform a series of rigorous quality control procedures on the observed data to obtain high-fidelity usable data. Firstly, the continuous observations of multiple fields over two months were divided into a series of one-hour datasets. Subsequently, stationarity and stratification stability parameters were calculated for each one-hour dataset. The stationarity of a time series was assessed using the relative non-stationarity parameter (*RNP*), which is defined as the relative difference between the variance of the entire time series and the mean variance of its 12 contiguous 5-minute subsequences. A time series is considered broadly stationary if $RNP \leq 0.3$ (Foken & Wichura 1996), and such series were used for the subsequent data analysis in this study. Notably, a time series is regarded as strongly stationary if all possible moments and joint moments remain invariant over time (Bendat & Piersol 2011). However, for atmospheric surface layer data, achieving strong stationarity is challenging due to diurnal variations (synoptic scale) and the limited occurrence of neutral stability conditions (Hutchins & Marusic 2007).

The stratification stability of the wind flow was evaluated using the Monin–Obukhov stability parameter, z/L . Here, $L = -\langle \Theta \rangle_t u_\tau^2 / (\kappa g \langle (w\theta)_t \rangle_0)$ is the Obukhov length, $\kappa = 0.41$ is the von Kármán constant, $g = 9.81 \text{ m s}^{-2}$ is gravitational acceleration, and $\langle (w\theta)_t \rangle_0$ represents the surface heat flux. As done in numerous previous studies (e.g. Klewicki, Priyadarshana & Metzger 2008; Hutchins *et al.* 2012; Chowdhuri, Kumar & Banerjee 2020), the friction velocity was calculated as $u_\tau = (\langle uw \rangle_t^2 + \langle vw \rangle_t^2)^{1/4}$ at $z = 1.5 \text{ m}$. When $|z/L| \leq 0.1$, the wind flow is approximately neutrally stratified, and thermal buoyancy effects are negligible (Kunkel & Marusic 2006).

Following the aforementioned data quality control procedures, nine sets of high-fidelity one-hour data were selected for analysis in this study, consisting of eight dust storm datasets and one clean-air dataset. The main parameters of these datasets are outlined in table 1. For the clean-air dataset, the mean electric field was negative (i.e. downward-pointing) with a magnitude of approximately 0.21 kV m^{-1} . In contrast, during dust storms, the mean electric field was positive (i.e. upward-pointing) and reached magnitudes of several tens of kilovolts per meter, indicating intense electrical activity.

Furthermore, the particle-to-air mass loading ratio (Φ_m) and the mean electrostatic Stokes number ($\overline{St_{el}}$) are used to quantify the importance of particle–turbulence and particle–electrostatics couplings, respectively, while the viscous Stokes number (St^+) is employed to assess the particle inertial effects. First, the particle-to-air mass loading ratio is defined as $\Phi_m = \rho_p / \rho_f \phi_V$, where ρ_p , ρ_f , and ϕ_V represent the particle mass density, air mass density, and particle volume fraction, respectively. It is well established that turbulence modulation by particles intensifies with increasing Φ_m , becoming prominent at $\Phi_m \sim O(0.1)$ (e.g. Kulick, Fessler & Eaton 1994; Yousefi *et al.* 2023). Second, the electrostatic Stokes number is defined as the ratio of the particle relaxation time scale, $\tau_p = d_p^2 \rho_p / (18\nu\rho_f)$ (Maxey 1987; Eaton & Fessler 1994), to the characteristic time scale of electrostatic interactions, $\tau_{el} = (6\pi \varepsilon_0 m_p / (nq^2))^{1/2}$ (Boutsikakis *et al.* 2022), expressed as $St_{el} = \tau_p / \tau_{el}$. Here, d_p , ν , ε_0 , m_p , n and q denote the particle diameter, air kinematic viscosity, vacuum permittivity, particle mass, particle number density, and particle electric

Data	Period	U_c (m s ⁻¹)	u_τ (m s ⁻¹)	$\langle\Theta\rangle_t$ (K)	$\langle C\rangle_t$ (mg m ⁻³)	$\langle E\rangle_t$ (kV m ⁻¹)	RNP	z/L ($\times 10^{-2}$)	Φ_m	$\overline{St_{el}}$	St^+
I	0428/14-15	8.56	0.47	292.75	0.61	10.03	0.13	-2.57	0.29	0.19	10.99
II	0428/15-16	9.31	0.53	293.86	0.90	11.12	0.11	-1.95	0.44	0.30	13.98
III	0429/16-17	10.13	0.57	299.72	1.28	7.91	0.11	-1.32	0.63	0.40	16.17
IV	0505/15-16	10.09	0.58	295.91	1.34	44.48	0.09	-0.01	0.66	0.55	16.74
V	0514/02-03	9.93	0.53	292.15	0.99	17.84	0.11	0.28	0.48	0.24	13.98
VI	0514/03-04	9.64	0.52	292.29	0.82	15.98	0.13	0.16	0.40	0.22	13.46
VII	0514/04-05	9.16	0.51	291.99	0.50	13.98	0.08	0.22	0.24	0.17	12.95
VIII	0514/05-06	8.92	0.49	291.82	0.56	12.77	0.09	0.19	0.27	0.18	11.95
IX	0423/23-24	6.18	0.30	283.12	—	-0.21	0.15	-0.06	—	—	—

Table 1. Overview of the used one-hour datasets. Here, ‘0428/14–15’ (similarity for others) denotes this dataset was taken on April 28, 2021 at 14: 00–15:00 UTC + 8, $U_c = \langle U \rangle_t$ is the convection velocity, u_τ is the friction velocity, $\langle \Theta \rangle_t$ is the mean ambient temperature, $\langle C \rangle_t$ is the mean PM10 dust concentration, $\langle E \rangle_t$ is the mean electric field, RNP is the relative non-stationarity parameter of the streamwise wind velocity, z/L is the Monin–Obukhov stability parameter of the wind flow, Φ_m is the particle-to-air mass loading ratio, $\overline{St_{el}}$ is the mean electrostatic Stokes number, and St^+ is the viscous Stokes number of the 10- μ m-diameter dust particles.

charge, respectively. The definition of τ_{el} is derived through dimensional analysis, assuming that τ_{el} is solely determined by ε_0 , m_p , n and q . Thus, the electrostatic Stokes number quantifies the relative importance of particle inertia compared to electrostatic forces: inter-particle electrostatic forces are negligible when St_{el} is very small, whereas these forces dominate particle dynamics when St_{el} is large. In this study, the average electrostatic effect among charged particles is characterised by the mean electrostatic Stokes number $\overline{St_{el}}$, taking into account only the particle class with the mean diameter. Third, the effects of particle inertia are evaluated using the viscous Stokes number, $St^+ \equiv \tau_p/\tau_v$, where $\tau_v = \nu/u_\tau^2$ represents the viscous time scale. Particles with a large St^+ are expected to exhibit quasi-ballistic behaviour, while those with a small St^+ tend to closely follow the fluid flow.

The estimation of the particle-to-air mass-loading ratio Φ_m and electrostatic Stokes number $\overline{St_{el}}$ is based on synchronous measurements of wind velocity, PM10 dust concentration and particle size distribution at 0.9 m height. Herein, several particle properties are used: (a) particle mass density is assumed to be 2650 kg m^{-3} , (b) the density and kinematic viscosity of the air are taken as 1.20 kg m^{-3} and $1.57 \times 10^{-5} \text{ m}^2 \text{ s}^{-1}$, respectively, and (c) the charge-to-mass ratio of particles is considered to have a typical value of $60 \text{ } \mu\text{C kg}^{-1}$ measured in dust storms (Schmidt *et al.* 1998; Zheng, Huang & Zhou 2003), although it may vary slightly from storm to storm. Further details regarding the estimation of Φ_m and $\overline{St_{el}}$ can be found in our previous study (Zhang & Zhou 2023). Figure 1 displays an example of the complete time series of the multiple fields in dataset II. It is shown that the multiple fields, particularly PM10 dust concentration and electric field, exhibit significant local intermittent behaviour, posing new demands on data processing methods, which is discussed in § 3.

3. Data analysis

3.1. Wavelet transform and wavelet PSD

Classical Fourier analysis represents data as a sum of trigonometric functions that extend to infinity, making it inefficient for dealing with local abrupt changes in multifield time series recorded in dust storms. In contrast, the use of a set of localised basis functions in wavelet transform allows us to unfold time series into the time and scale (or frequency) domain and, therefore, can uncover local intermittent events effectively (Daubechies 1992; Farge 1992; Torrence & Compo 1998; Zhou 2021). The continuous wavelet transform of a time series $\{x(t), t = 0, \dots, N - 1\}$ is defined as the convolution of $\{x(t)\}$ with a scaled and translated Morlet wavelet (Daubechies 1992; Torrence & Compo 1998),

$$W_x(t, \tau) = \sum_{t'=0}^{N-1} \sqrt{\frac{\delta_t}{\tau}} x(t') \overline{\psi_0} \left[\frac{(t' - t)\delta_t}{\tau} \right], \quad (3.1)$$

where t is the localised time index, τ is the wavelet scale that is inversely proportional to frequency f (i.e. $1/\tau = 1.03f$, see Torrence & Compo (1998) for the details), Morlet wavelet is expressed as $\psi_0(\eta) = \pi^{-1/4} e^{(i\omega_0\eta - \eta^2/2)}$ with dimensionless frequency $\omega_0 = 6$ satisfying the admissibility condition, $\overline{(\cdot)}$ denotes the complex conjugate, and δ_t is the sampling interval of the time series $\{x(t)\}$. Here, the discrete scales $\{\tau(j)\}$ are selected as fractional powers of two:

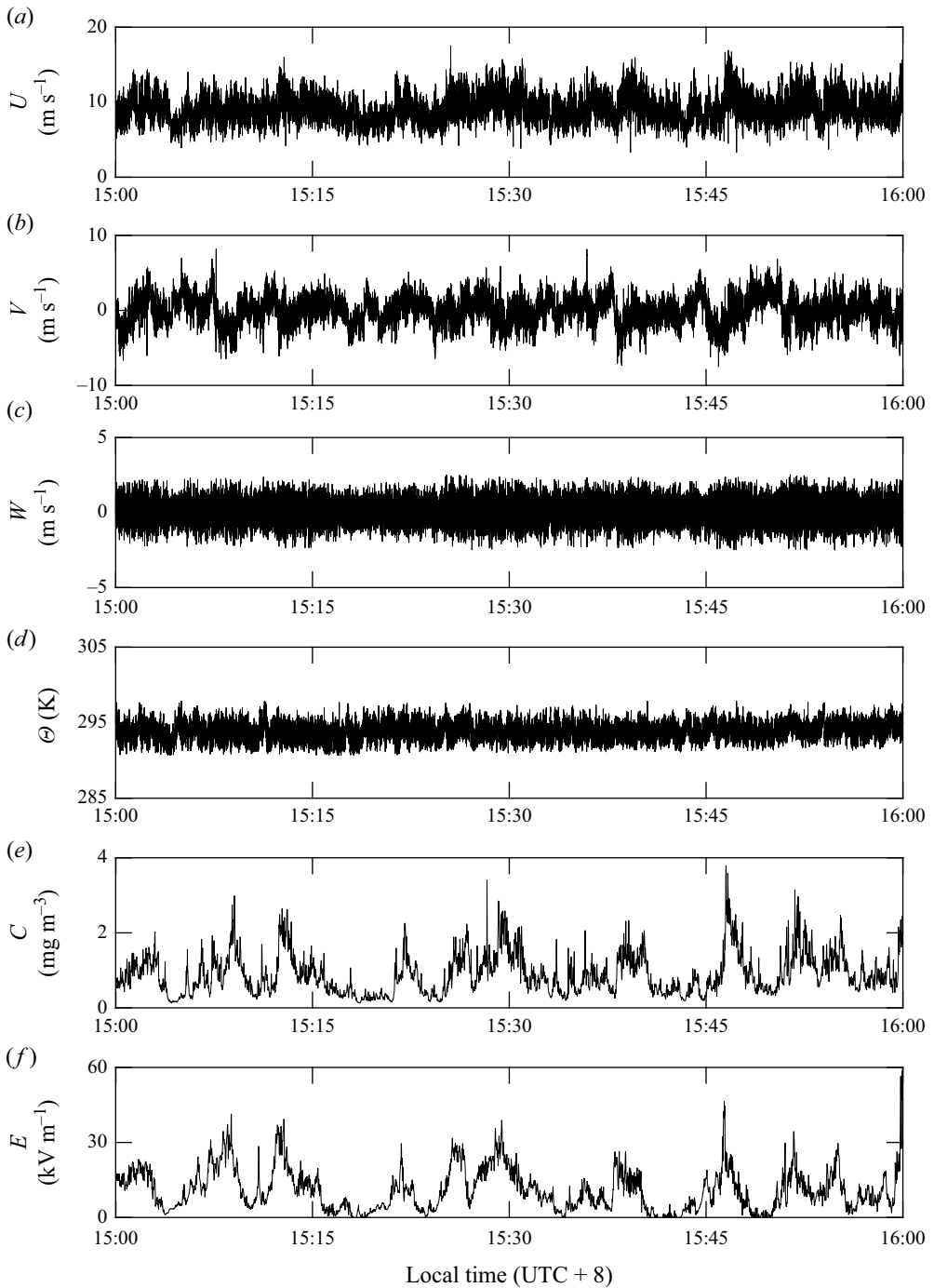


Figure 1. The complete data series of the dataset II. Panels (a–f) correspond to the streamwise (U), spanwise (V) and wall-normal (W) components of the wind velocity, ambient temperature (Θ), PM10 dust concentration (C), as well as electric field (E), respectively.

$$\tau(j) = \tau_0 2^{j\delta_j}, \quad j = 0, 1, \dots, J, \quad (3.2)$$

$$J = \delta_j^{-1} \log_2 \left(\frac{N\delta_t}{\tau_0} \right), \quad (3.3)$$

where $\tau_0 = 2\delta_t$ is the smallest resolvable scale, J determines the largest scale, and δ_j is the spacing between discrete scales.

As the square of a wavelet coefficient gives a fluctuating energy at a given time index t and scale τ , we thus define the local wavelet PSD of the time series $\{x(t)\}$ as (Farge 1992; Alexandrova *et al.* 2008; Ruppert-Felsot, Farge & Petitjeans 2009)

$$\psi_{xx}(t, \tau) = 2\delta_t |W_x(t, \tau)|^2. \quad (3.4)$$

The global wavelet PSD is given by

$$\phi_{xx}(\tau) = \langle \psi_{xx}(t, \tau) \rangle_t = \frac{1}{N} \sum_{t=0}^{N-1} \psi_{xx}(t, \tau), \quad (3.5)$$

where the time average $\langle \rangle_t$ is performed over the whole period. It is demonstrated that the global wavelet PSD corresponds to the smoothed Fourier PSD, providing an unbiased and consistent estimation of the true global PSD (Percival 1995; Torrence & Compo 1998).

3.2. Intermittency and coherent signature

Traditionally, the intermittency of a time series $\{x(t)\}$ at scale τ can be characterised by the non-Gaussian probability density function (PDF) of the field increment $\Delta x(t, \tau) = x(t + \tau) - x(t)$ between two time indexes t and $t + \tau$ (Frisch 1995; Pope 2000). Thanks to the fact that the real part of the wavelet coefficient $W_x(t, \tau)$ is proportional to the field increment $\Delta x(t, \tau)$ (Bernardini *et al.* 2023; Zhang *et al.* 2023), such deviations from the Gaussian PDF can be more conveniently measured by the wavelet flatness factor (Meneveau 1991; Camussi & Guj 1997; Alexandrova *et al.* 2008):

$$F_x(\tau) = \frac{\langle |W_x(t, \tau)|^4 \rangle_t}{\langle |W_x(t, \tau)|^2 \rangle_t^2}, \quad (3.6)$$

which quantifies the level of intermittency at scale τ . Notably, a Gaussian PDF corresponds to a wavelet flatness factor with a value of 3.

In contrast to wavelet flatness factor, the so-called local intermittency measure (LIM) (Farge 1992; Camussi & Guj 1997),

$$I_x(t, \tau) = \frac{|W_x(t, \tau)|^2}{\langle |W_x(t, \tau)|^2 \rangle_t}, \quad (3.7)$$

is defined by the ratio of local energy at the time index t and the scale τ to the time-averaged energy at the same scale and is generally used to quantify the level of local intermittency.

Based on LIM, it is convenient to extract time signatures of coherent structures from single-point measurements (Camussi & Guj 1997; Guj & Camussi 1999; Camussi *et al.* 2010). The basic idea is that intermittency is closely related to the strong field gradients (or field singularity) resulting from the passage of coherent structures. More specifically, the localised energetic coherent structures can be well projected onto a wavelet basis and thus are represented by sparse wavelet coefficients of large modules at a given time and scale (Salem *et al.* 2009; Camussi *et al.* 2010). In contrast, the random weak incoherent

components have wavelet coefficients extensively spread in the time and scale domain with a considerably smaller module compared to the coherent coefficients. Consequently, a large LIM could be considered as a result of coherent structures passing through the measurement points according to (3.7) (Camussi & Guj 1997; Guj & Camussi 1999; Camussi *et al.* 2008; Salem *et al.* 2009).

To clarify the relationships among the coherent structures of multiple fields in dust storms, a wavelet conditional average method is used to identify the phase-averaged coherent signatures of the wind velocity, PM10 dust concentration and electric field (Camussi & Guj 1997; Guj & Camussi 1999; Camussi 2002; Camussi & Di Felice 2006; Camussi *et al.* 2008; Salem *et al.* 2009; Camussi *et al.* 2010; Crawley *et al.* 2018). The coherent signatures of a time series are defined as the portions of the original time series (i.e. time series segments of appropriate width) that are centred around the energetic coherent structures. It is reasonably expected that LIM at scale τ_s larger than a threshold T_h are expected to correspond to the energetic coherent structures. Therefore, a set of time indices $\{t_0(i), i = 0, \dots, N_e - 1\}$ at which the coherent signatures are centred can be determined by

$$\{t_0(i)\} = \{t | I_x(t, \tau_s) > T_h, t = 0, \dots, N - 1\}, \quad (3.8)$$

where N_e is the number of the coherent signatures and τ_s is set to be τ_0 in order to obtain a better time resolution and statistical convergence of the conditional average (Camussi *et al.* 2010). In addition, the threshold LIM must be high enough, but not too high, so that only the most energetic coherent structures are detected and statistical convergence is achieved. A detailed discussion of the selection of threshold LIM T_h in the present study is provided in Appendix A. Apparently, a single coherent signature could be either positive or negative, but only positive LIM peaks are selected for identifying energetic signatures in the wavelet conditional average (Crawley *et al.* 2018).

Once the threshold LIM is selected, the i th extracted coherent signature $\{\tilde{x}_i(j), j = 0, \dots, \mathcal{E}\}$ can be explicitly expressed as

$$\tilde{x}_i(j) = x(t_0(i) - \mathcal{E}/2 + j), \quad (3.9)$$

where $\mathcal{E} + 1$ is the width of each extracted coherent signature.

The resulting phase-averaged coherent signature of time series $\{x(t)\}$ is accordingly written as

$$\langle \tilde{x} \rangle = \langle \tilde{x}_i(j) \rangle_{N_e} = \frac{1}{N_e} \sum_{i=0}^{N_e-1} \tilde{x}_i(j), \quad (3.10)$$

where $j = 0, \dots, \mathcal{E}$ and the ensemble average $\langle \rangle_{N_e}$ is taken over all extracted coherent signatures centred at $\{t_0(i)\}$. It is clear that the averaged coherent signature $\langle \tilde{x} \rangle$ represents the pattern of the most energetic coherent structures hidden in the original time series.

3.3. Wavelet coherence and linear coupling

To quantitatively assess the correlation between two time series $\{x(t)\}$ and $\{y(t)\}$, the cross wavelet transform W_{xy} can be introduced as (Hudgins, Friehe & Mayer 1993)

$$W_{xy}(t, \tau) = W_x(t, \tau) \overline{W_y}(t, \tau). \quad (3.11)$$

In analogy with the Pearson correlation coefficient, the wavelet coherence between two time series $\{x(t)\}$ and $\{y(t)\}$ is given by (Grinsted, Moore & Jevrejeva 2004; Camussi *et al.* 2008)

$$\gamma_{xy}^2(t, \tau) = \frac{|\mathcal{S}(W_{xy}(t, \tau))|^2}{\mathcal{S}(|W_x(t, \tau)|^2) \mathcal{S}(|W_y(t, \tau)|^2)}, \quad (3.12)$$

where \mathcal{S} is a smoothing operator in time and scale domain and can be used to build a balance between desired time and scale resolution and statistical significance (Grinsted *et al.* 2004). In this study, the smoothing operator is given by $\mathcal{S}(W) = \mathcal{S}_{scale}(\mathcal{S}_{time}(W(t, \tau)))$, where \mathcal{S}_{scale} and \mathcal{S}_{time} denote smoothing along the wavelet scale and time axis, respectively. Following Grinsted *et al.* (2004) and Camussi *et al.* (2008), we define the time-axis smoothing as $\mathcal{S}_{time}(W(t, \tau)) = W(t, \tau) * c_1 \exp(-t^2/(2\tau^2))$ at a fixed τ , and the scale-axis smoothing as $\mathcal{S}_{scale}(W(t, \tau)) = W(t, \tau) * c_2 \Pi(0.6\tau)$ at a fixed t . Here, the symbol $*$ denotes the convolution product, c_1 and c_2 are normalisation constants, and Π is the rectangle function. The scale smoothing is implemented using a boxcar filter with a width of 0.6. It is obvious that wavelet coherence $\gamma_{xy}^2(t, \tau)$ ranges from 0 to 1 and can be considered as a localised correlation coefficient in time and scale domain. In a system consisting solely of two interacting time series, wavelet coherence also represents a measure of the localised linear coupling between two time series (Ritz & Powers 1986; Narayanan & Hussain 1996; Bendat & Piersol 2011). When $\gamma_{xy}^2(t, \tau) = 1$, $\{x(t)\}$ and $\{y(t)\}$ are perfectly linearly coupled at time index t and scale τ .

It is straightforward to extend the concept of wavelet coherence to the case of multiple interacting time series, for example, $\{y(t)\}$, $\{x_1(t)\}$ and $\{x_2(t)\}$. In many situations, $\{y(t)\}$ (e.g. PM10 dust concentration) is coupled to both $\{x_1(t)\}$ and $\{x_2(t)\}$ (e.g. wind velocity and electric field). To uncover the ‘pure’ linear coupling between $\{y(t)\}$ and $\{x_1(t)\}$, one can define the partial wavelet coherence analogous to partial correlation as (Mihanović, Orlić & Pasarić 2009; Xiang & Qu 2018)

$$\gamma_{yx_1(x_2)}^2(t, \tau) = \frac{|\gamma_{yx_1}(t, \tau) - \gamma_{yx_2}(t, \tau)\overline{\gamma_{x_1x_2}}(t, \tau)|^2}{(1 - \gamma_{yx_2}^2(t, \tau))(1 - \gamma_{x_1x_2}^2(t, \tau))}, \quad (3.13)$$

where γ_{yx_1} (similarly for γ_{yx_2} and $\gamma_{x_1x_2}$) is given by

$$\gamma_{yx_1}(t, \tau) = \frac{\mathcal{S}(W_{yx_1}(t, \tau))}{\mathcal{S}(|W_y(t, \tau)|^2)^{1/2} \mathcal{S}(|W_{x_1}(t, \tau)|^2)^{1/2}}. \quad (3.14)$$

Accordingly, partial wavelet coherence $\gamma_{yx_1(x_2)}^2$ measures the localised linear coupling between $\{y(t)\}$ and $\{x_1(t)\}$ after excluding the influence of $\{x_2(t)\}$. Moreover, the multiple wavelet coherence defined by (Mihanović, Orlić & Pasarić 2009),

$$\gamma_{yx_1x_2}^2(t, \tau) = \frac{\gamma_{yx_1}^2(t, \tau) + \gamma_{yx_2}^2(t, \tau) - 2\text{Re}(\gamma_{yx_1}(t, \tau)\overline{\gamma_{yx_2}}(t, \tau)\overline{\gamma_{x_1x_2}}(t, \tau))}{1 - \gamma_{x_1x_2}^2(t, \tau)}, \quad (3.15)$$

can be used to account for the proportion of wavelet power of $\{y(t)\}$ at a time index t and scale τ explained by the linear relationship with $\{x_1(t)\}$ and $\{x_2(t)\}$. In (3.15), $\text{Re}()$ denotes the real part of a complex number.

Overall, as opposed to Fourier coherence, wavelet coherence and partial wavelet coherence provides a powerful tool to examine the localised linear coupling between two or three fields.

3.4. Wavelet bicoherence and quadratic nonlinear coupling

Aside from linear coupling, higher-order nonlinear couplings are undoubtedly broadband and significant in turbulent flows. In particular, frequency (or equivalently scale) components can interact with one another, generating new components at their sum (or difference) frequencies, known as combination components. In other words, the phases of the combination components are coupled to the primary interacting frequency pairs. This phenomenon goes by several different names including three-wave coupling, nonlinear triadic interactions and quadratic nonlinear (or phase) coupling but in each case the same basic mechanisms are involved.

Owing to the intermittent nature of turbulent fields, these phase couplings are not entirely filling in the time and frequency/scale space. In contrast to the Fourier bicoherence, which serves as a global phase coupling measure, the wavelet bicoherence can be used to detect the short-lived intermittent quadratic nonlinear coupling (Van Milligen, Hidalgo & Sanchez 1995; Lancaster *et al.* 2018). The wavelet auto-bicoherence of time series $\{x(t)\}$ over the period $t \in [0, N - 1]$ is defined by (Van Milligen *et al.* 1995; Schulte 2016)

$$b_{xxx}^2(\tau_1, \tau_2) = \frac{\left| \sum_{t=0}^{N-1} W_x(t, \tau_1) W_x(t, \tau_2) \overline{W_x(t, \tau)} \right|^2}{\left(\sum_{t=0}^{N-1} |W_x(t, \tau)|^2 \right) \left(\sum_{t=0}^{N-1} |W_x(t, \tau_1) W_x(t, \tau_2)|^2 \right)}, \tag{3.16}$$

where the frequency sum rule,

$$\frac{1}{\tau_1} + \frac{1}{\tau_2} = \frac{1}{\tau}, \tag{3.17}$$

is satisfied. The auto-bicoherence $b_{xxx}^2(\tau_1, \tau_2)$ determines the degree of quadratic nonlinear coupling among scales τ_1 , τ_2 and τ of time series $\{x(t)\}$ over the period $t \in [0, N - 1]$. By definition, wavelet auto-bicoherence is bounded between 0 and 1, with $b_{xxx}^2(\tau_1, \tau_2) = 0$ for independent random phase relationships, and $b_{xxx}^2(\tau_1, \tau_2) = 1$ for a maximum amount of coupling.

In turbulent flows, quadratic nonlinear couplings represent the nonlinear energy transfer among turbulent motions at scales τ_1 , τ_2 and τ , as well as the breakup of vortices (e.g. $\tau \rightarrow (\tau_1, \tau_2)$) and the formation of new vortices (e.g. $(\tau_1, \tau_2) \rightarrow \tau$) (Kim & Williams 2006). These processes ultimately lead to the redistribution of energy across different scales. Consequently, strong quadratic nonlinear couplings are indicative of notable spectral energy redistribution (Elgar & Guza 1985; Kim & Williams 2006; Bountin *et al.* 2008; Unnikrishnan & Gaitonde 2020), by means of both nonlinear energy transfer and the generation and disintegration of turbulent structures.

Similarly, the wavelet cross-bicoherence over the period $t \in [0, N - 1]$ can be defined as (Van Milligen *et al.* 1995; Lancaster *et al.* 2018)

$$b_{yxx}^2(\tau_1, \tau_2) = \frac{\left| \sum_{t=0}^{N-1} W_x(t, \tau_1) W_x(t, \tau_2) \overline{W_y(t, \tau)} \right|^2}{\left(\sum_{t=0}^{N-1} |W_x(t, \tau_1) W_x(t, \tau_2)|^2 \right) \left(\sum_{t=0}^{N-1} |W_y(t, \tau)|^2 \right)}, \tag{3.18}$$

which measures the degree of quadratic nonlinear coupling in the period $[0, N - 1]$ among scales τ_1 and τ_2 of $\{x(t)\}$ and scale τ of $\{y(t)\}$.

The wavelet cross-bicoherence can be also extended to the case of three coupled time series $\{x_1(t)\}$, $\{x_2(t)\}$ and $\{y(t)\}$ (e.g. Corke, Shakib & Nagib 1991; Corke *et al.* 2018; Arndt *et al.* 2020; Middlebrooks *et al.* 2024):

$$b_{y_{x_1 x_2}}^2(\tau_1, \tau_2) = \frac{\left| \sum_{t=0}^{N-1} W_{x_1}(t, \tau_1) W_{x_2}(t, \tau_2) \overline{W_y}(t, \tau) \right|^2}{\left(\sum_{t=0}^{N-1} |W_{x_1}(t, \tau_1) W_{x_2}(t, \tau_2)|^2 \right) \left(\sum_{t=0}^{N-1} |W_y(t, \tau)|^2 \right)}, \quad (3.19)$$

which is a measure the degree of quadratic nonlinear coupling in the period $[0, N - 1]$ among scale τ_1 of $\{x_1(t)\}$, scale τ_2 of $\{x_2(t)\}$ and scale τ of $\{y(t)\}$. Although the concept of partial wavelet coherence $\gamma_{y_{x_1(x_2)}}^2$ mentioned above can be used to extract the ‘pure’ linear coupling between $\{y(t)\}$ and $\{x_1(t)\}$ (or $\{x_2(t)\}$), we have no similar theory of partial wavelet bicoherence to isolate the ‘pure’ quadratic nonlinear coupling so far (McComas & Briscoe 1980; Van Milligen *et al.* 1995).

Furthermore, the wavelet summed bicoherence is defined as (Van Milligen *et al.* 1995)

$$B^2(\tau) = \frac{\sum b^2(\tau_1, \tau_2)}{\xi(\tau)}, \quad (3.20)$$

where the sum is taken over all τ_1 and τ_2 such that (3.17) is satisfied and $\xi(\tau)$ is the number of summands in the summation. By essentially aggregating or averaging the quadratic nonlinear couplings over multiple frequency pairs τ_1 and τ_2 , the summed bicoherence $B^2(\tau)$ provides insight into the overall strength or prevalence of the quadratic nonlinear couplings across the entire spectrum. Clearly, a higher summed bicoherence value suggests a stronger quadratic nonlinear coupling between frequency components at specific frequency combinations.

4. Results and discussion

4.1. Strong two-way particle–turbulence and particle–electrostatics couplings

We begin by determining the presence of strong two-way particle–turbulence and particle–electrostatics couplings in the eight dust storm datasets. Since particles are influenced by turbulence and the electric field is generated by moving charged particles, our objective is to explore whether dust particles introduce a significant feedback effect on turbulence and whether the electric field substantially affects particle transport.

First, these significant two-way couplings can be indirectly inferred from the large dimensionless parameters, Φ_m and St_{el} . At a height of 0.9 m, both Φ_m and St_{el} are estimated to reach approximately $O(0.1)$ (see table 1), indicating strong two-way couplings between particle–turbulence and particle–electrostatics, as suggested by the previously established criteria (Elghobashi 1994; Boutsikakis *et al.* 2022; Zhang *et al.* 2023).

Additionally, direct evidence is provided by examining how dust particles regulate turbulence statistics and how electrostatic effects influence PM10 dust concentration and vertical turbulent flux within a narrow range of friction velocity. Wall-normal profiles of the inner-scaled mean streamwise wind velocity and Reynolds shear stress are presented in figure 2. For comparison, the Reynolds stress documented by Hutchins *et al.* (2012) at the Surface Layer Turbulence and Environmental Science Test facility is also plotted in figure 2(b). Using the boundary layer thickness $\delta = 166 \pm 38$ m at the QLOA site (see Wang & Zheng 2016) and calculating the kinematic viscosity ν based on Sutherland’s law (Sutherland 1893), we find that the friction Reynolds number $Re_\tau \equiv u_\tau \delta / \nu$ varies from 3.44×10^6 to 6.72×10^6 for the eight dust storm datasets, which is consistent with the values reported by Hutchins *et al.* (2012). The strong consistency between the results of Hutchins *et al.* (2012) and the clean-air dataset indicates the high quality of the datasets

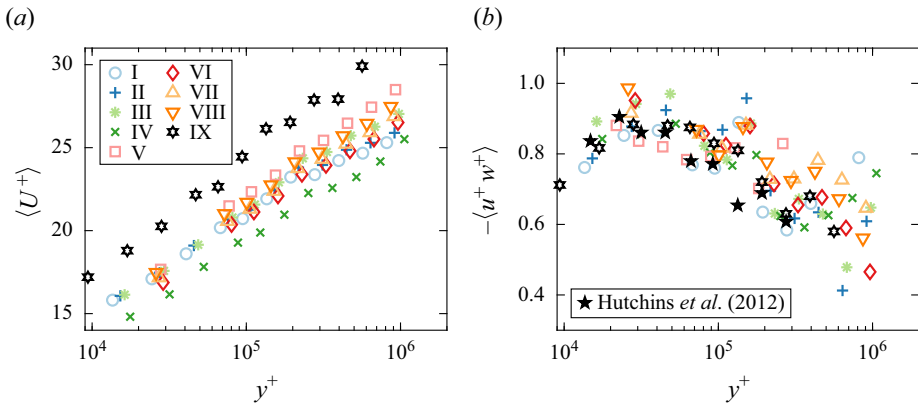


Figure 2. (a) Wall-normal profiles of the inner-scaled mean streamwise wind velocity $\langle U^+ \rangle = \langle U \rangle / u_\tau$. (b) Wall-normal profiles of the inner-scaled Reynolds shear stress $-\langle u^+ w^+ \rangle = -\langle uw \rangle / u_\tau^2$: black pentagrams denote the data from Hutchins *et al.* (2012), while other symbols represent current QLOA data.

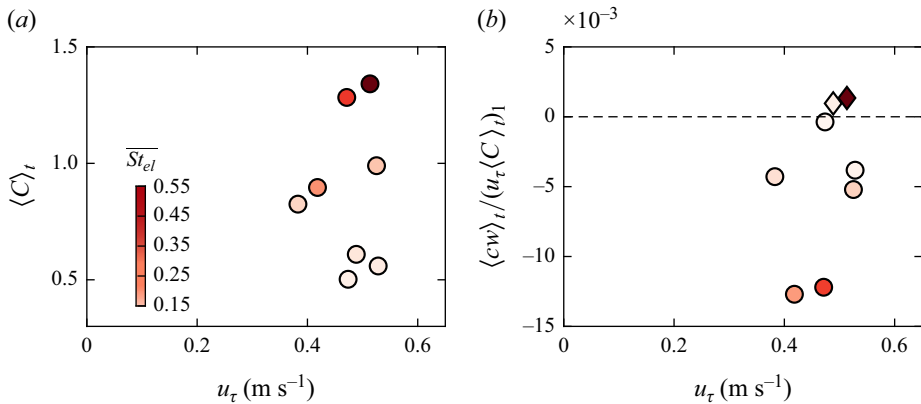


Figure 3. (a) Dependence of mean PM10 dust concentration on friction wind velocity (u_τ) and electrostatic Stokes number (\overline{St}_{el}). (b) Dependence of vertical turbulent dust flux on u_τ and \overline{St}_{el} , where the vertical turbulent dust flux $\langle cw \rangle_1$ is normalised by the product of friction velocity and the mean PM10 dust concentration from dataset I, denoted as $(u_\tau \langle C \rangle_1)_1$.

used herein. It is evident that the mean streamwise velocity and Reynolds stress for both clean-air and dust storm datasets fairly follow a logarithmic law. However, compared to the clean-air dataset, the dust storm datasets exhibit lower inner-scaled mean streamwise wind velocity and relatively higher inner-scaled Reynolds stress (especially for $y^+ \gtrsim O(10^5)$), suggesting a substantial feedback effect of dust particles on wind flow (figure 2b).

On the other hand, figure 3(a,b) illustrate the dependence of mean PM10 dust concentration and vertical turbulent dust flux on friction wind velocity and electrostatic Stokes number for the eight dust storm datasets. Since the friction Reynolds numbers of these data are nearly identical (i.e. $u_\tau = 0.53 \pm 0.04$ m s⁻¹), the variations in the concentration and vertical turbulent dust flux of the PM10 dust particles are primarily caused by electrostatic effects. A clear increasing trend in mean PM10 dust concentration is observed with respect to the electrostatic Stokes number (figure 3a), suggesting that inter-particle electrostatic forces facilitate the lifting of particles from sandy surfaces.

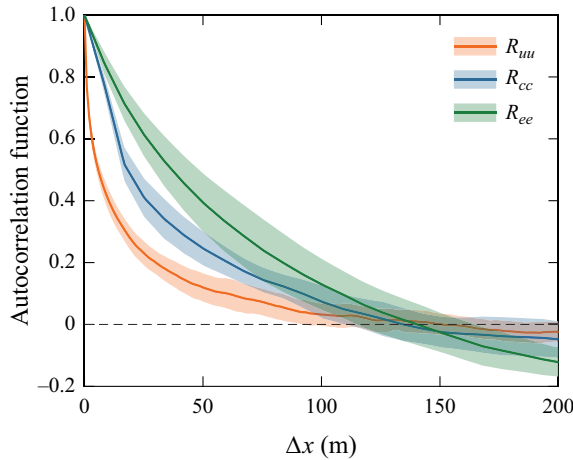


Figure 4. Autocorrelation functions for the fluctuating streamwise wind velocity, PM10 dust concentration and electric fields. Solid lines represent the mean autocorrelation functions calculated from eight dust storm datasets. The shaded areas indicate the standard deviations of the autocorrelation functions across these datasets.

In addition, [figure 3\(b\)](#) shows both positive (upward) and negative (downward) vertical turbulent dust fluxes, which correspond to the processes of dust dispersal into the air and dust redeposition onto the surface, respectively (Shao 2008). In both cases, the magnitude of the vertical turbulent dust flux tends to increase with the electrostatic Stokes number, indicating that electrostatic effects tend to enhance vertical turbulent dust flux. In short, a significant two-way coupling between particles and electrostatics is evident in the analysed datasets.

In addition to the first- and second-order one-point statistics, the two-point longitudinal autocorrelation functions of the fluctuating streamwise wind velocity, PM10 dust concentration and electric fields are calculated as,

$$R_{AA}(\Delta x) = \frac{\langle A(x)A(x + \Delta x) \rangle}{\sigma_{A(x)}\sigma_{A(x+\Delta x)}}, \quad (4.1)$$

where $A \in \{u, c, e\}$ and the longitudinal separation Δx is obtained from the time lag Δt using Taylor’s hypothesis of frozen turbulence, i.e. $\Delta x = \Delta t U_c$. As shown in [figure 4](#), the autocorrelation functions exhibit long tails, extending to distances of up to approximately 300 m (only the positive part is shown due to symmetry), which is equivalent to twice the boundary layer thickness. These non-zero correlations at large separations indicate the presence of large-scale coherent structures in wind velocity, PM10 dust concentration, and electric fields. The underlying physical mechanism is that if a large structure is present, there will be some degree of correlation between the motions at different points across the boundary layer region that the structure spans. The autocorrelation functions thus provide insight into the average picture of these large-scale coherent structures.

It is important to stress that the existence of large-scale coherent structures in the electric fields suggests conspicuous charge separation on a large scale comparable with boundary-layer thickness, as electric fields are directly related to space charge density according to Coulomb’s law. This large-scale charge separation can be explained by the tendency of smaller, low-inertia, negatively charged particles to accumulate in specific regions of the instantaneous turbulence field (Eaton & Fessler 1994), while larger, high-inertia, positively

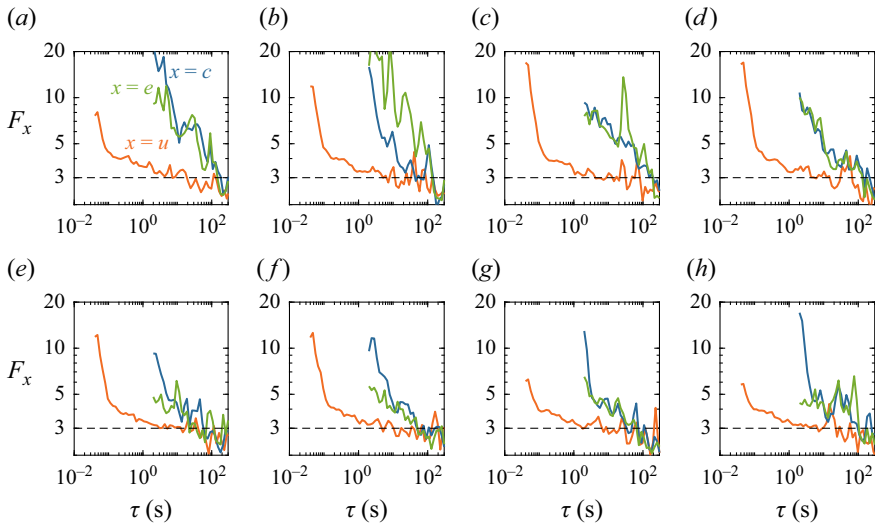


Figure 5. Wavelet flatness F_x of the fluctuating streamwise wind velocity ($x = u$), PM10 dust concentration ($x = c$) and electric field ($x = e$) for datasets from (a) I to (h) VIII.

charged particles are distributed more uniformly, as previously reported (Di Renzo & Urzay 2018; Zhang & Zhou 2020).

4.2. Multifield local intermittent behaviour

As previously mentioned, the multiple fields in dust storms exhibit conspicuous intermittent behaviour in the time domain (figure 1), whose time-averaged characteristics can be quantified through wavelet flatness factor. Figure 5 compares the wavelet flatness factor of the streamwise wind velocity, PM10 dust concentration and electric field at various scales for the used eight dust storm datasets (table 1). It can be seen that, at larger scales (i.e. $\tau \sim 10^2$ s), the multifield wavelet flatness factor is close to 3, indicating that the PDFs of the multiple field increments obey a Gaussian distribution and the multiple fields are non-intermittent at larger scales. However, as the scale decreases, the multifield wavelet flatness factor increases, suggesting a super-Gaussian PDFs of the field increments and presence of intermittency at smaller scales. Importantly, the wavelet flatness factor of PM10 dust concentration and electric field is nearly identical but greater than that of the streamwise wind velocity, especially at smaller scales. This multifield intermittency behaviour near the surface differs from that far away from the surface, where the intermittency is strongest for PM10 dust concentration, followed by the electric field, and weakest for wind velocity (Zhang *et al.* 2023).

Next, the localised intermittent behaviour for multiple fields is assessed using LIM. As exemplified in figure 6, it depicts the multifield LIM for dataset II. Due to the higher sampling frequency of wind velocity compared to PM10 dust concentration and electric field, the LIM for streamwise wind velocity is presented across broader scales than that for PM10 dust concentration and electric field (i.e. $\tau \in [0.04, 2]$ s, corresponding to the shaded area in figure 6(a)). It is important to emphasise that the magnitude of the sampling frequency only affects the smallest resolvable scale in the LIM graph but does not change the LIM distribution in the time domain. It is clear that all LIMs do not completely fill the time and scale domain, becoming increasingly fragmented as the scale decreases. Within the entire resolved scale range of one-Hertz data $\tau \in [2, 1.5 \times 10^3]$ s, the overall LIM

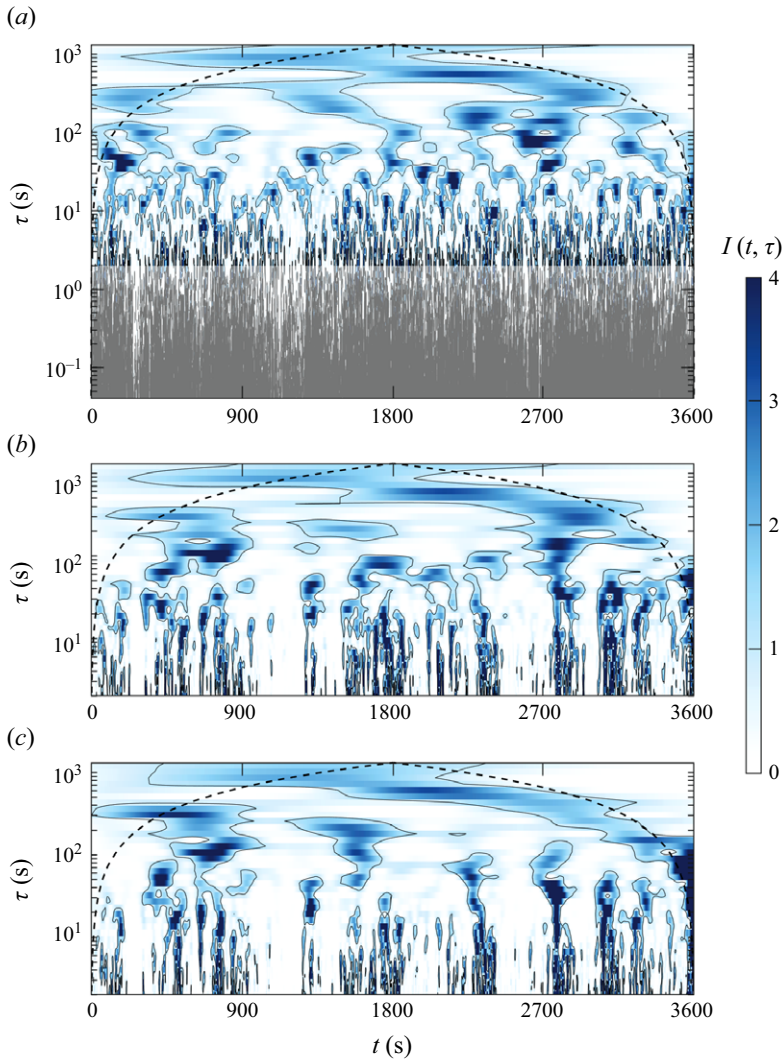


Figure 6. LIMs of the fluctuating (a) streamwise wind velocity, (b) PM10 dust concentration and (c) electric field for dataset II. The upper region enclosed by the black dashed line and the coordinate axes represents the ‘cone of influence’, where edge effects become significant. The black contour denotes the 95 % confidence level for white noise.

patterns for PM10 dust concentration and electric field behave very similarly. At larger scales (i.e. $\tau \in [1 \times 10^2, 1.5 \times 10^3]$ s), all LIMs display similar behaviour, particularly showing high values over a broad time window as a result of an energetic synoptic-scale motion passing through the measurement point. However, the LIM for PM10 dust concentration and electric field appears sparser than that for streamwise wind velocity at smaller scales (i.e. $\tau \in [2, 1 \times 10^2]$ s). Similar conclusions can be drawn for other datasets, albeit not presented here for clarity.

To gain further insight, the proposed wavelet conditional average method (i.e. equation (3.8)) is utilised to isolate the phase-averaged coherent signatures of the multiple fields in dust storms. The fundamental principle behind this method is that peaks in the LIM distribution correspond to the passage of energetic structures. Therefore, when

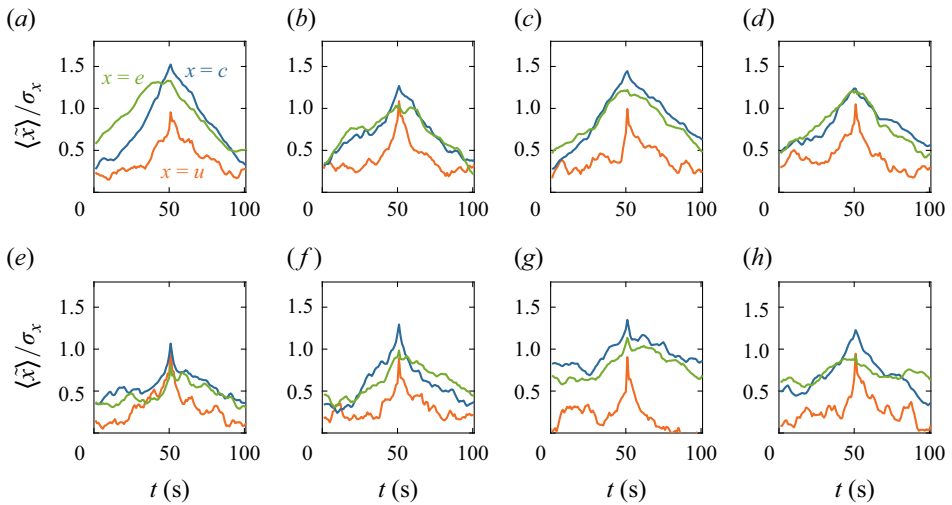


Figure 7. Phase-averaged coherent signatures of the fluctuating streamwise wind velocity ($x = u$), PM10 dust concentration ($x = c$) and electric field ($x = e$) for datasets from (a) I to (h) VIII. The phase-averaged coherent signatures are normalised by the corresponding standard deviations of the original time series $\{x(t)\}$, i.e. $\langle \tilde{x} \rangle / \sigma_x$.

the LIM, $I(t, \tau_0)$, exceeds a certain threshold value, it is believed to indicate the presence of energetic coherent structures. It is evident that the selection of the threshold LIM is crucial for extracting coherent signatures. In this study, we set the threshold LIM to 2 (see Appendix A), consistent with previous studies (e.g. Camussi & Guj 1997). It is worth emphasising that, for the sake of comparing different physical fields, we subsampled the wind velocity data to 1 Hz when extracting coherent signals (hence, $\tau_0 = 2$ s). Figure 7 illustrates the phase-averaged coherent signatures extracted from all datasets, which are normalised with respect to the standard deviation of the original time series. Because only positive LIM peaks were utilised, the phase-averaged coherent signatures are all positive within a 100-second duration and exhibit a ‘A’ shape. Clearly, such ‘A-shaped’ coherent signatures for multiple fields display highly similar temporal characteristics. In particular, the coherent signatures of PM10 dust concentration and electric field are shown to collapse well, but they are stronger than those of the streamwise wind velocity.

An important question that warrants further exploration is why the coherent signatures of PM10 dust concentration and electric fields are more pronounced compared to those of wind velocity. A plausible physical explanation is the presence of multiscale ramp-cliff structures in the time series of PM10 dust concentration and electric fields, which produce stronger gradients and, consequently, increased intermittency. Both time series in figure 1(e,f) clearly exhibit a gradual rise (the ramp) followed by a sharp drop (the cliff). In certain instances, this order reverses, featuring a steep increase followed by a more gradual decline. Together, these two patterns are referred to as ramp-cliff structures (Buaria *et al.* 2021). Their characteristic time scales range from a few seconds to several hundred seconds, displaying typical multiscale behaviour in atmospheric boundary layer flow (Belušić & Mahrt 2012). To understand the origin of these structures, we examine the transport equation for PM10 dust concentration:

$$\frac{\partial C}{\partial t} + U_{p,j} \frac{\partial C}{\partial x_j} = \Gamma_C \frac{\partial^2 C}{\partial x_j^2}, \quad (4.2)$$

where $U_{p,j}$ and Γ_C denote the j th ($j = 1, 2, 3$) component of the velocity of the dust particles and the diffusion coefficient, respectively (Warhaft 2000; Shao 2008). In (4.2), when the particle inertia, gravitational settling and electrostatic effects are negligible, $U_{p,j}$ can be replaced by the wind velocity U_j because the relative particle-fluid velocity becomes zero. Notably, this equation is devoid of a pressure term, indicating that the PM10 dust concentration field undergoes large-scale deformation solely through convective processes. In contrast to the velocity field, the essential local isotropisation and mixing effects of pressure are absent in the PM10 dust concentration field. Consequently, PM10 dust concentration can be expelled from the core regions of vortical structures and accumulate along the periphery or at stagnation points, leading to the formation of ramp-cliff structures (Watanabe & Gotoh 2004). These structures generate steep gradients associated with intense dissipation, thereby enhancing intermittency. With respect to electric fields, previous studies have also demonstrated a close correspondence between the structures of electric fields and PM10 dust concentration (Di Renzo & Urzay 2018; Zhang 2024), as electric fields are entirely generated by charged dust particles and are therefore determined by their spatial and temporal distribution. Furthermore, from a structural stability perspective, the most intermittent structures in PM10 dust concentration and electric fields manifest as two-dimensional sheet-like structures (Zhang *et al.* 2023), which are inherently less stable than the filamentary intermittent structures in the velocity field. Thus, the generation and annihilation of these sheet-like structures occur more frequently, resulting in intense fluctuations in both PM10 dust concentration and electric fields (Chen & Cao 1997).

4.3. Multifield linear coupling

In dust storms, the presence of interactions between particles and turbulence, as well as between particles and electrostatics, indicates that PM10 dust concentration is influenced by both turbulent flows and electric fields. In such cases, the wavelet coherence between PM10 dust concentration and wind velocity (or electric field) cannot represent the ‘pure’ linear coupling relationship between them. In this study, the ‘pure’ linear couplings between two interacting fields are assessed using partial wavelet coherence (i.e. equation (3.13)). Figure 8 displays the partial wavelet coherences $\gamma_{cw(e)}^2$ and $\gamma_{ce(w)}^2$ for dataset II, along with their time-averaged (i.e. $\langle \gamma_{cw(e)}^2 \rangle_t$ and $\langle \gamma_{ce(w)}^2 \rangle_t$) and scale-averaged (i.e. $\langle \gamma_{cw(e)}^2 \rangle_\tau$ and $\langle \gamma_{ce(w)}^2 \rangle_\tau$) values. Here we focus on multifield couplings in the vertical direction, because the distribution of PM10 dust concentration is mainly determined by its vertical transport processes (Zheng 2009; Zhang & Liu 2023), which is also demonstrated in drifting snow (Paterna *et al.* 2016). Notably, w is subsampled to 1 Hz to match the sampling frequency of c and e . The disparity between the time-averaged wavelet coherence and partial wavelet coherence is discussed in detail in Appendix B.

When $\tau \lesssim 30$ s, $\gamma_{cw(e)}^2$ and $\gamma_{ce(w)}^2$ display elongated, intermittent, strikes along the scale axis (figure 8*b,e*). This indicates a broadband and intermittent linear coupling behaviour between PM10 dust concentration and vertical wind velocity, as well as between PM10 dust concentration and electric field. However, when $\tau \gtrsim 30$ s, $\gamma_{cw(e)}^2$ and $\gamma_{ce(w)}^2$ no longer exhibit pronounced intermittent behaviour. While sporadic high linear couplings between PM10 dust concentration and vertical wind velocity occur at larger scales, their linear coupling strength remains weak across most time and scale domains. In contrast, PM10 dust concentration and electric field display very high coupling throughout scales above approximately 200 s. This discrepancy in linear coupling at large scales is further reflected in the time-averaged partial wavelet coherence. From figure 8(*c,f*), it can be seen that

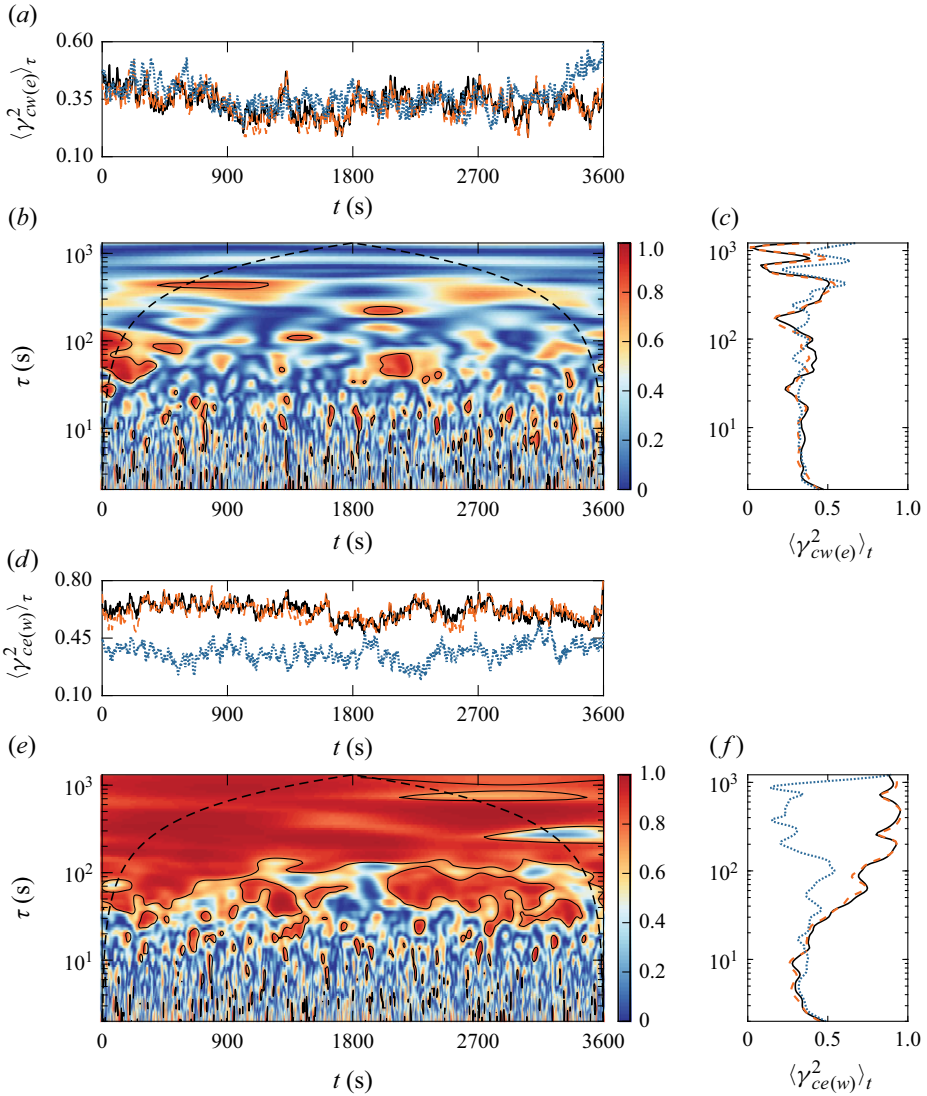


Figure 8. (a) Scale-averaged partial wavelet coherences $\langle \gamma_{cw(e)}^2 \rangle_\tau$ for the raw (black solid line), intermittent (orange dashed line) and non-intermittent (blue dotted line) components of dataset II. (b) Partial wavelet coherence between the raw PM10 dust concentration and the vertical wind velocity component $\gamma_{cw(e)}^2$. (c) Time-averaged partial wavelet coherences for the raw (black solid line), intermittent (orange dashed line) and non-intermittent (blue dotted line) components of dataset II. (d–f) Same as (a–c) but for partial wavelet coherences between PM10 dust concentration and electric field. In (b,e), the upper region enclosed by the black dashed line and the coordinate axes represents the ‘cone of influence’, where edge effects become significant. The black contour denotes the 95 % confidence level for white noise.

$\langle \gamma_{cw(e)}^2 \rangle_t$ and $\langle \gamma_{ce(w)}^2 \rangle_t$ are almost identical for $\tau \lesssim 10$ s. However, with increasing scale, $\langle \gamma_{cw(e)}^2 \rangle_t$ remains constant, while $\langle \gamma_{ce(w)}^2 \rangle_t$ rapidly increases, reaching its maximum value at $\tau \approx 200$ s.

To examine whether multifield intermittency plays an important role in the intermittent linear coupling behaviour, we decompose the raw time series of wind velocity, PM10 dust

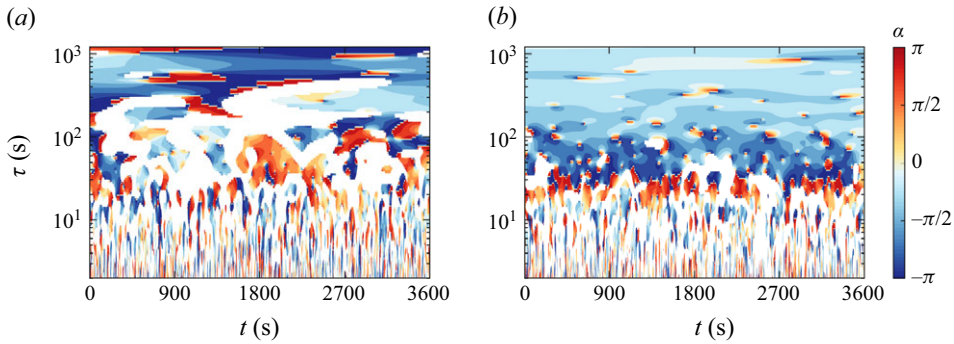


Figure 9. Phase angle between the intermittent components of (a) PM10 dust concentration and vertical wind velocity, as well as (b) PM10 dust concentration and electric field for dataset II. For clarity, the phase angle is conditioned on wavelet coherence greater than 0.25.

concentration and electric field into a coherent component and a background incoherent component. We then investigate the partial wavelet coherence and phase angle between these components. Following the approach proposed by Farge and co-workers (e.g. Farge, Pellegrino & Schneider 2001; Ruppert-Felsot *et al.* 2009), the decomposition process is as follows: (i) apply a continuous wavelet transform to the raw time series to obtain the wavelet coefficients; (ii) coefficients whose modulus exceeds F times their standard deviation at the same scale are regarded as associated with energetic coherent structures and are subsequently used to reconstruct the coherent component through a conditioned inverse wavelet transform. In contrast, the remaining coefficients, with relatively smaller moduli, correspond to the incoherent component. In this study, the threshold value F is set to 1, because the resulting scaling exponent of the structure function for the incoherent component fully recovers the Kolmogorov’s self-similarity law (Zhang *et al.* 2023). Thus, through this procedure, the decomposed coherent and incoherent components are intermittent and non-intermittent, respectively.

Figures 8(a,d) and 8(c,f) compare the scale- and time-averaged partial wavelet coherences of the raw series, as well as intermittent and non-intermittent components for dataset II. It is shown that the scale- and time-averaged partial wavelet coherences of the non-intermittent components remain largely invariant with respect to both time and scale. These values are typically small and exhibit significant discrepancies when compared to those of the raw series. This suggests that the non-intermittent components display a weak, yet noticeable, intermittent multifield linear coupling behaviour across the entire time and scale domains. On the contrary, the scale- and time-averaged partial wavelet coherences of the intermittent components closely match those of the raw series, indicating that the intermittent components dominate the multifield linear coupling behaviour, rather than the non-intermittent components.

Since the coupling behaviour is closely related to the phase angle between two interacting time series, we also present the phase angle between the intermittent components of PM10 dust concentration and vertical wind velocity, as well as between PM10 dust concentration and electric field, in figure 9. The phase angle between time series $\{x(t)\}$ and $\{y(t)\}$, α_{xy} , is computed as

$$\alpha_{xy} = \arctan \left(\frac{\Im(W_{xy})}{\Re(W_{xy})} \right), \quad (4.3)$$

where $\Im()$ and $\Re()$ denote the imaginary and real parts of a complex number, respectively.

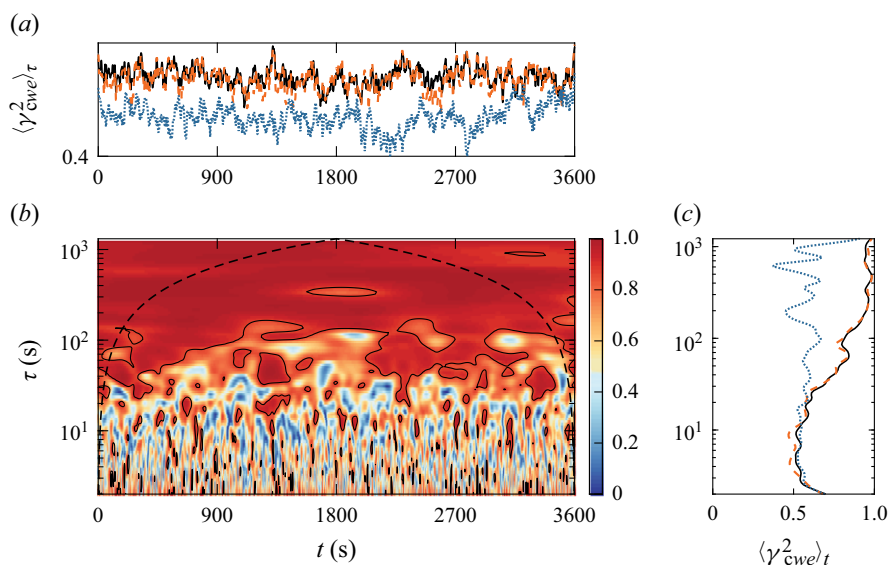


Figure 10. (a) Scale-averaged multiple wavelet coherences $\langle \gamma_{cwe}^2 \rangle_t$ for the raw (black solid line), intermittent (orange dashed line) and non-intermittent (blue dotted line) components of dataset II. (b) Multiple wavelet coherence among the raw PM10 dust concentration, vertical wind velocity and electric field γ_{cwe}^2 . (c) Time-averaged multiple wavelet coherences $\langle \gamma_{cwe}^2 \rangle_t$ for the raw (black solid line), intermittent (orange dashed line) and non-intermittent (blue dotted line) components. In (b), the upper region enclosed by the black dashed line and the coordinate axes represents the ‘cone of influence’, where edge effects become significant. The black contour denotes the 95 % confidence level for white noise.

Throughout the entire time and scale domain of figure 9(a), and for $\tau \lesssim 30$ s in figure 9(b), the phase angle is nearly constant across scales but exhibits alternating positive and negative values over time. This behaviour, referred to as a phase-unlocked pattern, corresponding to the weak coupling regions identified in figure 8(c,f). Such a weak and phase-unlocked coupling pattern can be attributed to the high multifield intermittency at small scales (figure 5). High intermittency corresponds to short-lived, sporadic and intense fluctuations, which make it difficult to establish a systematic and organised relationship among different fields. However, for larger scales in figure 9(b) ($\tau \gtrsim 100$ s), the phase angle remains nearly constant with scale and time, indicative of perfect ‘phase synchronisation’. In these regions, the linear coupling strength exceeds 0.8. The emergence of strong, phase-locked coupling at larger scales is closely associated with the presence of similar multifield large-scale coherent structures (see figure 4). These identical coherent structures, which are thought to dominate the coupling behaviour, are reasonably expected to produce strong coupling and give rise to phase synchronisation. Note that this positive correlation between coupling strength and phase synchronisation is a well-established feature of chaotic systems (Boccaletti *et al.* 2002), and it has now been observed in the complex dust storm turbulence.

Besides the ‘pure’ linear coupling between two interacting fields, the combined contribution of vertical wind velocity and electric field to PM10 dust concentration is explored using multiple wavelet coherence, as presented in figure 10. It is evident that the overall pattern of γ_{cwe}^2 resembles that of $\gamma_{ce(w)}^2$, but with higher time-averaged values (figure 10b). On average, more than 50 % and 95 % of the power of PM10 dust concentration can be accounted for by the linear relationship with vertical wind velocity

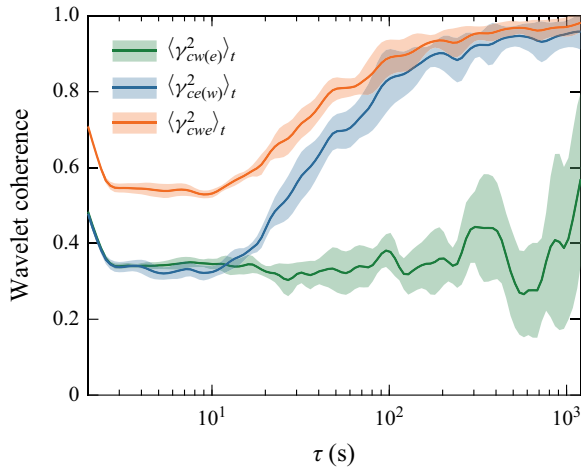


Figure 11. Comparison of partial wavelet coherence and multiple wavelet coherence for all eight dust storm datasets. Solid lines denote the mean wavelet coherence, where $\langle \rangle_t$ denotes average over time. Shaded areas indicate the standard deviations of the time-averaged wavelet coherences across the eight datasets.

and electric field at $\tau \lesssim 30$ s and $\tau \gtrsim 200$ s, respectively (figure 10c). Also, multiple wavelet coherence appears to be dominated by the multifield intermittent components.

In addition, a detailed comparison of partial wavelet coherence and multiple wavelet coherence for all eight dust storm datasets is shown in figure 11. It is evident that the differences in time-averaged partial wavelet coherence and multiple wavelet coherence among the eight datasets are considerably small (i.e. very narrow shadowed areas in figure 11). From figures 8 and 11, we conclude that when $\tau \lesssim 10$ s, the linear coupling behaviours between PM10 dust concentration and vertical wind velocity $\gamma_{cw(e)}^2$, as well as between PM10 dust concentration and electric field $\gamma_{ce(w)}^2$, are similar, displaying broadband and intermittent behaviours. Within this scale range, PM10 dust concentration is jointly influenced by vertical wind velocity and electric field. When $\tau \gtrsim 10$ s (especially $\gtrsim 100$ s), however, the linear coupling between PM10 dust concentration and electric field $\gamma_{ce(w)}^2$ significantly outweighs that of PM10 dust concentration and vertical wind velocity $\gamma_{cw(e)}^2$, indicating the dominance of the electric field in influencing PM10 dust concentration. This finding is in agreement with the results presented in figure 3, where PM10 dust concentration and vertical turbulent dust flux increase significantly with the electrostatic Stokes number. Furthermore, the multiple wavelet coherence being smaller than unity suggests that PM10 dust concentration cannot be perfectly explained by linear combined couplings with wind velocity and electric field alone, perhaps indicating a significant role played by nonlinear couplings (Narayanan & Hussain 1996).

4.4. Multifield PSD and quadratic nonlinear coupling

As stated in § 3.4, wavelet auto-bicoherence is believed to play a role in spectral energy redistribution. Therefore, we attempted to interpret the multifield global wavelet PSDs through the analysis of wavelet auto-bicoherence. Figure 12 shows the multifield global wavelet PSDs for all eight dust storm datasets. It is clear that the global wavelet PSDs for the eight datasets are nearly collapsed onto a single curve (figure 12a), suggesting identical spectral characteristics among the different datasets. Although the sampling frequency of PM10 dust concentration and the electric field is much lower than that of

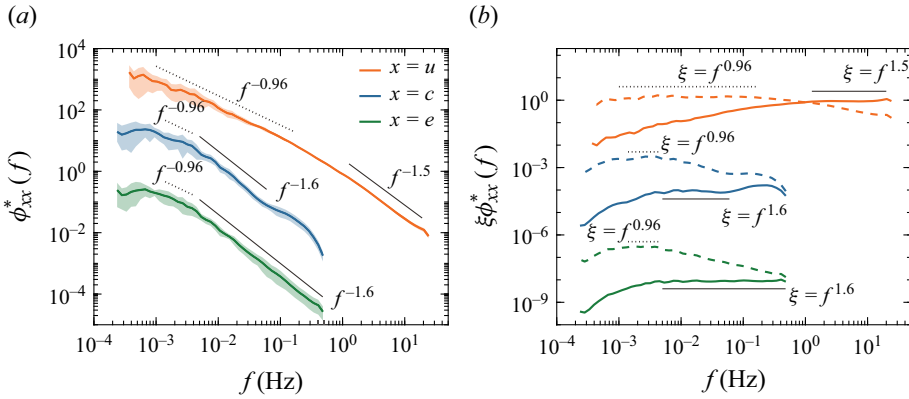


Figure 12. (a) Global wavelet PSDs of the streamwise wind velocity, PM10 dust concentration and electric field, where $\phi_{uu}^*(f) = \phi_{uu}(f)/u_\tau^2$, $\phi_{cc}^*(f) = \phi_{cc}(f)/\langle c^2 \rangle$ and $\phi_{ee}^*(f) = \phi_{ee}(f)/\langle e^2 \rangle$. Lines and shaded areas denote the mean and standard deviations for eight dust storm datasets. (b) Compensated wavelet PSDs of the corresponding multiple fields (standard deviations are not shown), where the horizontal dotted and solid lines represent the frequency ranges of the power-law spectra. Note that, $\phi_{cc}(f)$, $\phi_{ee}(f)$ and their compensated spectra are vertically shifted for clarity.

wind velocity, the global wavelet PSDs of all physical fields exhibit two distinct spectral regions: they show power laws with exponents of $\sim f^{-0.96}$ in the low-frequency region, a break at the intermediate frequencies, and steeper power laws with exponents of $\sim f^{-1.5}$ or $\sim f^{-1.6}$ in the high-frequency region. The former power law is consistent with the ‘complete similarity’ scaling f^{-1} (Nickels *et al.* 2005) and the latter one is in line with the Kolmogorov scaling $f^{-5/3}$ (Kolmogorov 1941). These spectral behaviours are clearly observable in the compensated PSDs (figure 12b). The f^{-1} power law of the streamwise velocity can be derived from the inviscid theory of Perry, Henbest & Chong (1986), in which both inner scaling, $\phi_{uu}(k_x z)/u_\tau^2 = \phi_{uu}(k_x)/(z u_\tau^2) = f(k_x z)$, and outer scaling, $\phi_{uu}(k_x \delta)/u_\tau^2 = \phi_{uu}(k_x)/(\delta u_\tau^2) = f(k_x \delta)$, are simultaneously valid in an overlap region (Nickels *et al.* 2005; Hwang, Hutchins & Marusic 2022). Here, $k_x = 2\pi f/U_c$ represents the streamwise wavenumber, and δ denotes the boundary layer thickness. Such overlap arguments are consistent with Townsend’s attached eddy hypothesis (Marusic & Monty 2019).

Wind tunnel experiments conducted by Nickels *et al.* (2005) and the refined model proposed by Hwang *et al.* (2022) demonstrated that a well-developed f^{-1} spectrum should be observed not only at a high Reynolds number but also very close to the surface. In the present study, the friction Reynolds number $Re_\tau \equiv u_\tau \delta/\nu$ varies from 3.44×10^6 to 6.72×10^6 and z/δ lies in the range of [0.0044, 0.007] for the eight dust storm datasets, satisfying the aforementioned criteria (Nickels *et al.* 2005; Hwang *et al.* 2022).

It is noteworthy that the streamwise velocity follows the power law f^{-1} across the frequency range from $\sim 10^{-3}$ to $\sim 10^{-1}$ Hz, spanning two decades long. Such a wide scaling provides convincing evidence of the complete similarity. In addition to the streamwise velocity, PM10 dust concentration and electric field also exhibit a power law with an index of -1 , but their length is only about 1/3 of a decade. As indicated by (4.2), the observed difference in the f^{-1} spectral bandwidth is likely due to the distinct transport (excluding pressure effects) and dissipation (influenced by both viscous and molecular diffusion) characteristics of PM10 dust concentration compared to those of wind velocity, although a quantitative analysis of the underlying physical mechanisms has not yet been conducted here. The emergence of a f^{-1} for PM10 dust concentration and electric field

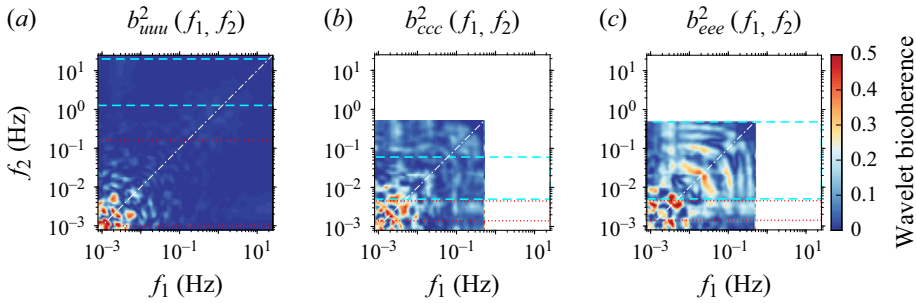


Figure 13. Wavelet auto-bicoherence of the (a) streamwise wind velocity, (b) PM10 dust concentration and (c) electric field for dataset II. The frequency intervals between the two horizontal dotted and dashed lines correspond to the f^{-1} and $f^{-5/3}$ scaling, respectively. The dot-dashed lines denote the axis of symmetry of the bicoherence.

suggests that ‘complete similarity’ can be probably extended to multiple fields in dust storms. Furthermore, the streamwise velocity, PM10 dust concentration and electric field exhibit a Kolmogorov-like $f^{-5/3}$ power law in the high-frequency region, although their specific frequency ranges are different. The Kolmogorov-like $f^{-5/3}$ power laws of PM10 dust concentration and the electric field can be explained by a phenomenological theory based on the Kolmogorov-style analysis of the local-in-wavenumber-space cascade of the variances of PM10 dust concentration and space-charge density (Zhang & Zhou 2023). Within the framework of the variance cascade, the PSD of PM10 dust concentrations (or space-charge density) is assumed to be solely determined by wavenumber and the dissipation rates of the PM10 dust concentration variance (or space-charge density variance) and turbulent energy. A standard dimensional analysis yields a Kolmogorov-like $-5/3$ power law for PM10 dust concentration and a $1/3$ power law for space-charge density. Using the PSD relationship between space-charge density and electric field, we also obtain the $-5/3$ power law for the electric field. In other words, the $-5/3$ power-law spectral range of PM10 dust concentration and electric field does not necessarily coincide with that of wind velocity.

More importantly, although the spectral breakpoints of PM10 dust concentration and electric field are essentially identical, they are much lower than those of the streamwise wind velocity. As depicted in figure 12(b), the spectral breakpoints of PM10 dust concentration and electric field occur at approximately 4×10^{-3} Hz, while those of streamwise wind velocity emerge at around 0.2–1 Hz. To interpret such a discrepancy in spectral breaks, we quantify the multifield wavelet auto-bicoherence $b_{xxx}^2(\tau_1, \tau_2)$, where $x \in \{u, c, e\}$, as quadratic nonlinear couplings are believed to be responsible for the spectral energy redistribution in terms of frequency combinations (Elgar & Guza 1985; Bountin *et al.* 2008; Unnikrishnan & Gaitonde 2020). In the literature, bicoherence are typically assessed in the frequency domain for convenience (e.g. Elgar & Guza 1985; Corke, Shakib & Nagib 1991; Van Milligen *et al.* 1995; Kim & Williams 2006; Bountin *et al.* 2008; Craig *et al.* 2019; Unnikrishnan & Gaitonde 2020; Paquin *et al.* 2024). Therefore, the resulting bicoherence in this article is also presented as a function of frequency.

As shown in figure 13, the wavelet auto-bicoherences of all physical fields peak within the region of $f_1 + f_2 \leq 2 \times 10^{-2}$ Hz. However, beyond this region, the wavelet auto-bicoherence of streamwise wind velocity approaches 0, while those of PM10 dust concentration and electric field exceed 0.1. Particularly, the local peaks of the electric field

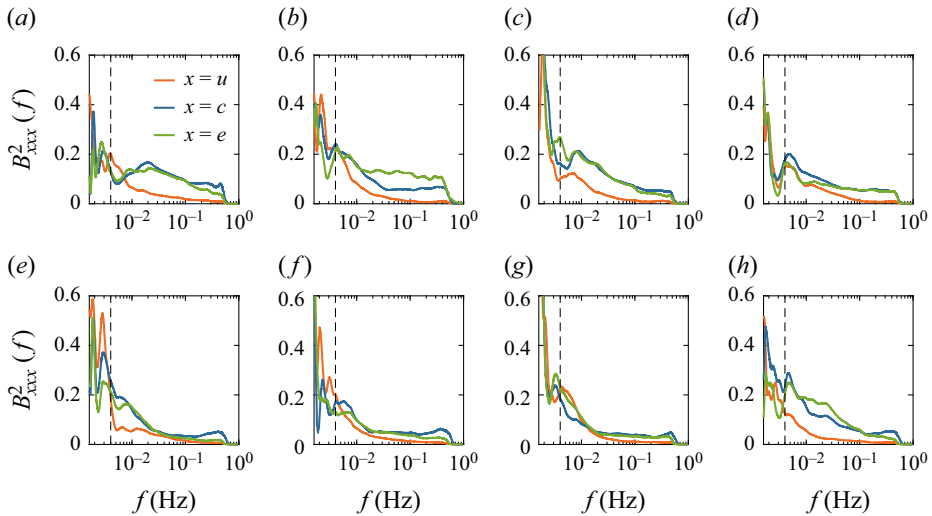


Figure 14. Wavelet summed auto-bicoherence of the fluctuating streamwise wind velocity ($x = u$), PM10 dust concentration ($x = c$) and electric field ($x = e$) for datasets from (a) I to (h) VIII. The vertical dashed lines mark $f = 4 \times 10^{-3}$ Hz.

around $f_1 = 0.03$ and $f_2 = 0.1$ reach 0.3. This indicates that, compared to streamwise wind velocity, PM10 dust concentration and electric field exhibit strong quadratic nonlinear coupling over a wider range of scales. Importantly, because bicoherence can also be interpreted as an indication of the energy cascade between scales (Cui & Jacobi 2021), we believe that such broader and stronger quadratic nonlinear couplings lead to the broadening of the Kolmogorov $-5/3$ power-law spectrum, in line with figure 12. As discussed in § 3.4, the physical processes responsible for the broadening of the $-5/3$ power-law spectrum of PM10 dust concentration and electric field involve intense nonlinear energy transfer and the generation and breakdown of turbulent motions across various scales satisfying frequency sum rule (3.17) (Kim & Williams 2006; Bountin *et al.* 2008; Unnikrishnan & Gaitonde 2020).

To further verify this argument, we present the wavelet summed auto-bicoherence analysis in figure 14, which represents the overall strength of quadratic nonlinear couplings across the entire spectrum. Clearly, the wavelet summed auto-bicoherence for multiple fields decreases with increasing frequency. When $f \lesssim 4 \times 10^{-3}$ Hz, the wavelet summed auto-bicoherence for all fields is nearly the same. However, when $f \gtrsim 4 \times 10^{-3}$ Hz, the wavelet summed auto-bicoherence of the streamwise wind velocity is much lower than that of PM10 dust concentration and electric field. This consistency between the transition point of wavelet summed auto-bicoherence and spectral breakpoints indicates that quadratic nonlinear coupling is indeed the primary physical mechanism determining the differences in global wavelet PSDs among multiple physical fields (e.g. Elgar & Guza 1985; Bountin *et al.* 2008; Cui & Jacobi 2021).

Apart from wavelet auto-bicoherence, we also evaluate the wavelet cross-bicoherence among multiple fields in order to unveil the interphase quadratic nonlinear coupling. As an example, figure 15 displays the wavelet cross-bicoherence among multiple fields for dataset II. Again, because PM10 dust concentration is mainly determined by the vertical transport of dust particles, we thus evaluate the wavelet cross-bicoherence between PM10 dust concentration, vertical wind velocity and electric field herein. Unlike the

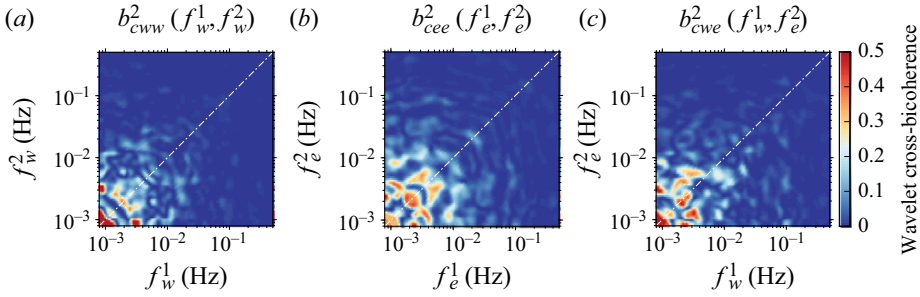


Figure 15. Wavelet cross-bicoherence (a) between PM10 dust concentration and vertical wind velocity b_{cww}^2 , (b) between PM10 dust concentration and electric field b_{cee}^2 , and (c) between PM10 dust concentration, vertical wind velocity and electric field b_{cwe}^2 for dataset II. The dot-dashed lines denote the axis of symmetry of the cross-bicoherence, except for b_{cwe}^2 .

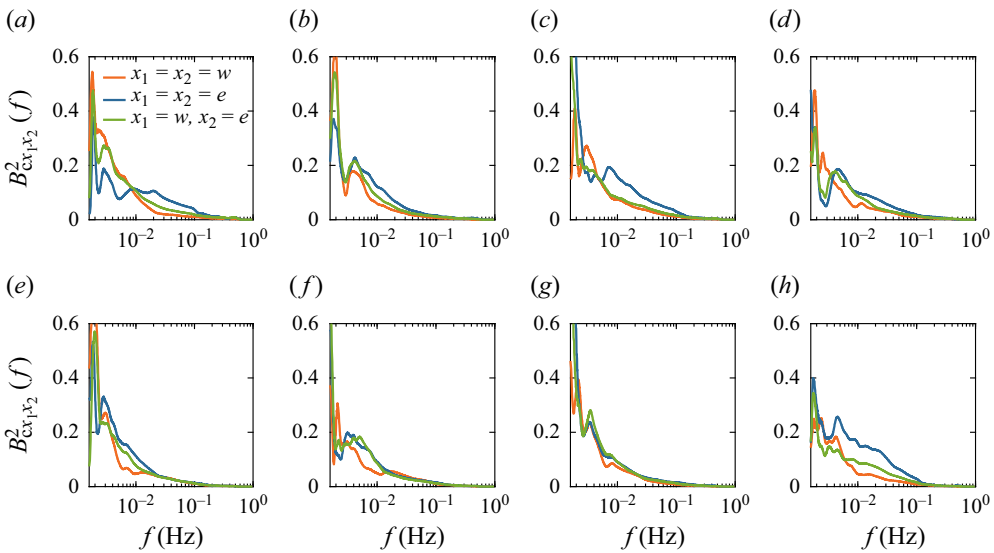


Figure 16. Wavelet summed cross-bicoherence between the fluctuating multiple fields for datasets from (a) I to (h) VIII. Here, w , c and e denote the fluctuating vertical wind velocity, PM10 dust concentration and electric field, respectively.

wavelet auto-bicoherence of multiple physical fields, the wavelet cross-bicoherences b_{cww}^2 , b_{cee}^2 and b_{cwe}^2 are conspicuous in the region of $f_1 + f_2 \lesssim 2 \times 10^{-2}$ Hz, where $(f_1, f_2) = \{(f_w^1, f_w^2), (f_e^1, f_e^2), (f_w^1, f_e^2)\}$, with values outside this region being very small. This indicates that strong interphase quadratic nonlinear coupling (e.g. wavelet cross-bicoherences larger than 0.1) occurs only in the low-frequency (large-scale) region. Specifically, the b_{cwe}^2 values in the upper and lower triangular areas are no longer symmetric about the diagonal, suggesting that the interphase quadratic nonlinear coupling between PM10 dust concentration and electric field differs from that between PM10 dust concentration and vertical wind velocity. Similarly, the comparison of interphase quadratic nonlinear coupling, especially in the high-frequency region where wavelet cross-bicoherence is not easily compared, can be more clearly demonstrated in the corresponding

wavelet summed cross-bicoherence. Overall, in the high-frequency region (e.g. $f > 10^{-2}$), B_{cee}^2 is the largest, followed by B_{cwe}^2 , and B_{cww}^2 is the weakest (figure 16), indicating that interphase quadratic nonlinear coupling at high frequencies (small scales) is mainly dominated by the interaction between PM10 dust concentration and electric field.

5. Conclusions

Dust storms are an extremely high-Reynolds number flows involving turbulence–particle–electrostatics couplings, serving as a natural laboratory for studying complex particle-laden flows. Although our previous study (Zhang *et al.* 2023) has revealed the properties of multifield intermittency in dust storms, the linear and quadratic coupling characteristics of multiple fields remain unknown. To remedy this problem, we conducted a series of joint measurements of such multiple fields at a height of 0.9 m above the surface at the Qingtu Lake Observation Array. After performing a rigorous data quality control process, we obtained eight sets of high-fidelity, stationary, near-neutral dust storm data, each spanning one hour. It is shown that the magnitude of the particle-to-air mass loading ratio and electrostatic Stokes number are of the order of 0.1, and the statistics of the wind velocity (mean streamwise velocity and Reynolds stress) and PM10 dust particles (mean mass concentration and vertical turbulent flux) are altered dramatically, indicating the presence of strong particle–turbulence and particle–electrostatics couplings.

Given the notable intermittency of multiple fields in dust storms, on the basis of continuous wavelet transform, we performed the following analyses: (a) employing the local intermittency measure (LIM) and LIM-based wavelet conditional average method to elucidate the localised intermittency of multiple fields; (b) utilising wavelet coherence, partial wavelet coherence and multiple wavelet coherence analysis of the raw data and their non-intermittent and intermittent components to explore the localised linear coupling between PM10 dust concentration and wind velocity, as well as between PM10 dust concentration and electric field; (c) applying auto-bicoherence to clarify the discrepancies in the breakpoints of the global wavelet PSDs of the streamwise wind velocity compared to those of the PM10 dust concentration and electric field; and (d) using cross-bicoherence analysis to unveil the interphase quadratic nonlinear coupling among multiple fields. Our main findings are listed below.

- (i) The time-averaged intermittency of multiple fields increases with decreasing scale, showing a consistent trend for PM10 dust concentration and electric field but a relatively slow change for streamwise wind velocity. This behaviour contrasts with the weak coupling regime, where the intermittency is most pronounced in PM10 dust concentration, followed by the electric field, and is weakest in wind velocity (Zhang *et al.* 2023). Additionally, multiple fields exhibit a ‘ Δ -shaped’ phase-averaged coherent signature in the time domain, with the amplitude being the same for PM10 dust concentration and electric field but larger than that for streamwise wind velocity. Such more energetic coherent signatures for PM10 dust concentration and electric field are perhaps resulted from their multiscale ramp-cliff structures in the time domain.
- (ii) The localised linear coupling behaviour is found to be dominated by the intermittent component of the raw time series. At scales $\tau \lesssim 30$ s, alongside the phase-unlocked pattern, the ‘pure’ linear couplings between PM10 dust concentration and vertical wind velocity, as well as between PM10 dust concentration and electric field in the time and scale domain, are notably intermittent because of high intermittency.

They exhibit an elongated, streaked pattern along the scale axis and their time-averaged linear coupling strengths are nearly the same. At scales $\tau \gtrsim 30$ s, due to the presence of very similar multifield large-scale coherent structures, PM10 dust concentration and electric field are significantly linearly coupled across the entire time and scale domain and exhibit a phase synchronisation phenomenon, with the time-averaged linear coupling strength exceeding 0.95 when $\tau \gtrsim 200$ s. However, PM10 dust concentration and vertical wind velocity display sporadic high linear coupling, resulting in the time-averaged linear coupling strength remaining at approximately a constant value of 0.32. This implies that at small scales, PM10 is jointly determined by wind speed and the electric field, whereas at large scales, it is dominated by the electric field. Considering the combined linear contribution from vertical wind velocity and electric field, more than 50 % and 95 % of the power of PM10 dust concentration at $\tau \lesssim 30$ s and $\tau \gtrsim 200$ s, respectively, can be explained.

- (iii) The global wavelet power spectral densities (PSDs) of multiple fields show a power law with a -1 slope at low frequencies, a breakpoint at $\sim 4 \times 10^{-3}$ Hz for PM10 dust concentration and electric field but within $\sim [0.2, 1]$ Hz for streamwise wind velocity, and a steeper power law at higher frequencies with a $-5/3$ slope. The emergence of well-developed f^{-1} PSDs for PM10 dust concentration and electric field suggests that, in addition to wind velocity, the ‘complete similarity’ argument (Nickels *et al.* 2005; Hwang *et al.* 2022) may also be extended to multiple fields in dust storms. The distinct spectral breakpoint of streamwise wind velocity, compared to that of PM10 dust concentration and electric field, can be attributed to its relatively narrow band and weak quadratic nonlinear coupling. This weak coupling is associated with spectral energy redistribution through nonlinear energy transfer and the generation and breakdown of turbulent motions across different scales. (Elgar & Guza 1985; Bountin *et al.* 2008; Unnikrishnan & Gaitonde 2020; Cui & Jacobi 2021). Furthermore, interphase quadratic nonlinear coupling appears to be strong only at larger scales, while it is weak at smaller scales, with the interaction between PM10 dust concentration and electric field being dominant.

Funding. This work was supported by the National Natural Science Foundation of China (grant numbers 12388101, 12472252 and 92052202) and the Fundamental Research Funds for the Central Universities (grant number lzujbky-2021-ey19).

Declaration of interests. The authors report no conflict of interests.

Appendix A. Selection of the threshold LIM

As mentioned in § 3.2, the local intermittency measure (LIM) of the time series $\{x(t), t = 0, \dots, N - 1\}$, $I_x(t, \tau)$, is defined as the ratio of local energy $|W_x(t, \tau)|^2$ to the time-averaged energy $\langle |W_x(t, \tau)|^2 \rangle_t$ at scale τ , serving as a measure of the local intermittency at time index t and scale τ . Since intermittency is associated with the passage of coherent structures (Camussi & Guj 1997; Chowdhuri, Iacobello & Banerjee 2021), the magnitudes of LIM at the smallest resolvable scale τ_0 can be thresholded to extract a set of coherent signatures, as described in (3.8). The threshold LIM T_h is a crucial parameter that determines the level of intermittency of the extracted coherent signatures. It must be sufficiently high to detect only the most energetic events yet not excessively high, allowing enough events to be detected for statistical convergence to be reached (Grassucci *et al.* 2015). Figure 17 illustrates the effects of varying the threshold LIM T_h on the extracted phase-averaged coherent signatures of the multiple fields for dataset II. It is observed that

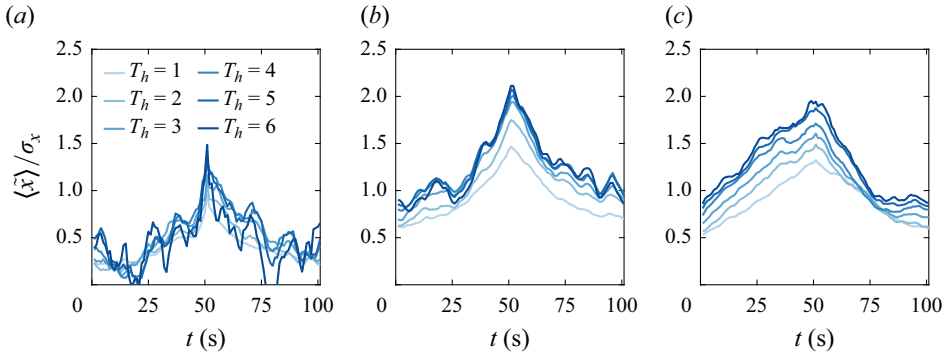


Figure 17. Phase-averaged coherent signatures of (a) streamwise wind velocity ($x = u$), (b) PM10 dust concentration ($x = c$) and (c) electric field ($x = e$) for dataset II as a function of threshold LIM T_h . The phase-averaged coherent signatures are normalised by the corresponding standard deviations of the time series σ_x .

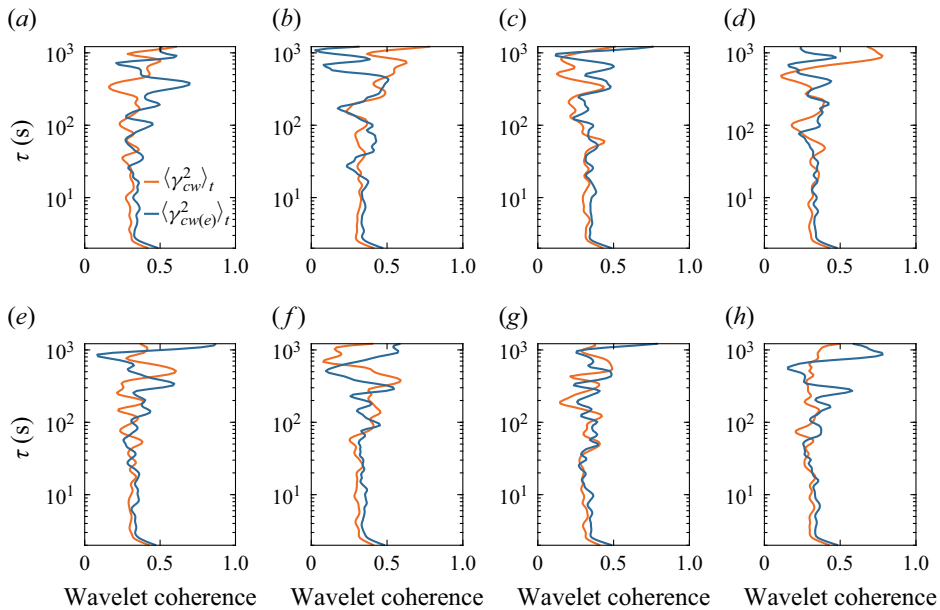


Figure 18. Comparison of time-averaged wavelet coherence $\langle \gamma_{cw}^2 \rangle_t$ and partial wavelet coherence $\langle \gamma_{cw(e)}^2 \rangle_t$ for datasets from (a) I to (h) VIII.

as the threshold LIM T_h increases from one to six, the magnitudes of the multifield phase-averaged coherent signatures increase, albeit with very similar patterns. This suggests that selecting T_h within the range of [1, 6] does not significantly alter the conclusions presented herein. Consequently, the threshold LIM is set to a constant value of two for all physical fields and datasets, consistent with previous studies (e.g. Camussi & Guj 1997).

Appendix B. Disparity between the wavelet coherence and partial wavelet coherence

In dust storms, the transportation of charged PM10 dust particles is mainly determined by aerodynamic and electrostatic forces, with the gravitational effect being relatively small (Zhang & Zhou 2023). Consequently, PM10 dust concentration is coupled with both

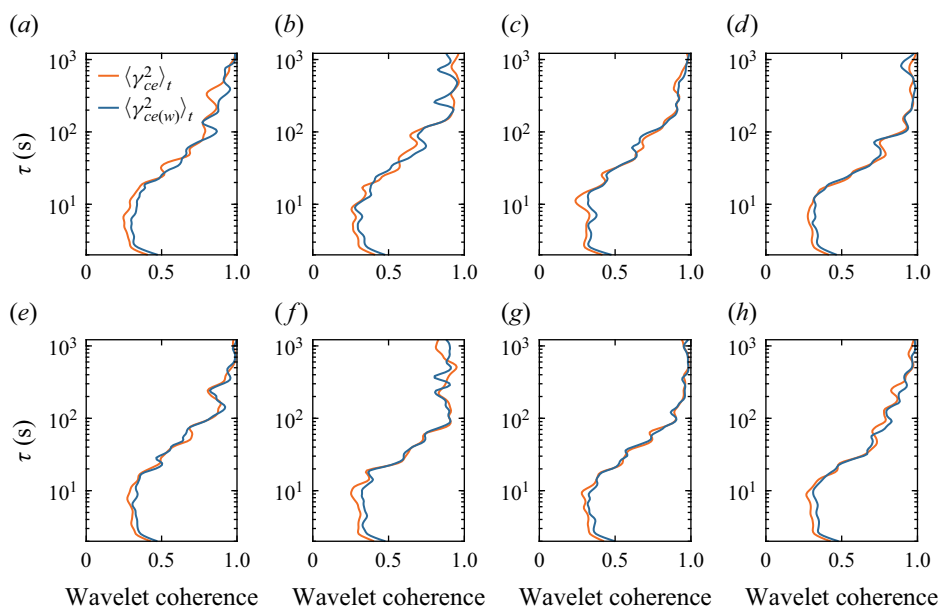


Figure 19. Comparison of time-averaged wavelet coherence $\langle \gamma_{ce}^2 \rangle_t$ and partial wavelet coherence $\langle \gamma_{ce(w)}^2 \rangle_t$ for datasets from (a) I to (h) VIII.

vertical wind velocity and electric field. The traditional wavelet coherence γ_{cw}^2 (or γ_{ce}^2), defined by (3.12), can only characterise the apparent linear coupling between PM10 dust concentration and vertical wind velocity (or electric field), without revealing the strength of the linear coupling between them alone. In contrast, the partial wavelet coherence $\gamma_{cw(e)}^2$ (or $\gamma_{ce(w)}^2$), defined by (3.13), removes the influence of the electric field (or wind velocity), thus allowing us to isolate the pure linear coupling between PM10 dust concentration and vertical wind velocity (or electric field). Figures 18 and 19 respectively present the comparison between time-averaged wavelet coherence and partial wavelet coherence for PM10 dust concentration and vertical wind velocity, as well as for PM10 dust concentration and electric field. Notably, significant differences exist between time-averaged wavelet coherence and partial wavelet coherence. In particular, within small-scale ranges (i.e. $\tau < 10$ s), the time-averaged partial wavelet coherence is notably greater than the time-averaged wavelet coherence, underscoring the necessity of considering partial wavelet coherence.

REFERENCES

ALEXANDROVA, O., CARBONE, V., VELTRI, P. & SORRISO-VALVO, L. 2008 Small-scale energy cascade of the solar wind turbulence. *Astrophys. J.* **674** (2), 1153–1157.

AGNON, Y. & SHEREMET, A. 1997 Stochastic nonlinear shoaling of directional spectra. *J. Fluid Mech.* **345**, 79–99.

ARNDT, A., CORKE, T., MATLIS, E. & SEMPER, M. 2020 Controlled stationary/travelling cross-flow mode interaction in a Mach 6.0 boundary layer. *J. Fluid Mech.* **887**, A30.

BALACHANDAR, S. & EATON, J.K. 2010 Turbulent dispersed multiphase flow. *Annu. Rev. Fluid Mech.* **42** (1), 111–133.

BELUŠIÁ, D. & MAHRT, L. 2020 Is geometry more universal than physics in atmospheric boundary layer flow? *J. Geophys. Res.-Atmos.* **117**, D09115.

BENDAT, J.S. & PIERSON, A.G. 2011 *Random Data: Analysis and Measurement Procedures*. John Wiley & Sons.

- BERNARDINI, M., DELLA POSTA, G., SALVADORE, F. & MARTELLI, E. 2023 Unsteadiness characterisation of shock wave/turbulent boundary-layer interaction at moderate Reynolds number. *J. Fluid Mech.* **954**, A43.
- BIFERALE, L., MUSACCHIO, S. & TOSCHI, F. 2012 Inverse energy cascade in three-dimensional isotropic turbulence. *Phys. Rev. Lett.* **108** (16), 164501.
- BOCCALETTI, S., KURTHS, J., OSIPOV, G., VALLADARES, D.L. & ZHOU, C.S. 2002 The synchronization of chaotic systems. *Phys. Rep.* **366** (1–2), 1–101.
- BOUNTIN, D., SHIPLYUK, A. & MASLOV, A. 2008 Evolution of nonlinear processes in a hypersonic boundary layer on a sharp cone. *J. Fluid Mech.* **611**, 427–442.
- BOUTSIKAKIS, A., FEDE, P. & SIMONIN, O. 2022 Effect of electrostatic forces on the dispersion of like-charged solid particles transported by homogeneous isotropic turbulence. *J. Fluid Mech.* **938**, A33.
- BRANDT, L. & COLETTI, F. 2022 Particle-laden turbulence: progress and perspectives. *Annu. Rev. Fluid Mech.* **54** (1), 159–189.
- BUARIA, D., CLAY, M.P., SREENIVASAN, K.R. & YEUNG, P.K. 2021 Small-scale isotropy and ramp-cliff structures in scalar turbulence. *Phys. Rev. Lett.* **126** (3), 034504.
- CAMUSSI, R. 2002 Coherent structure identification from wavelet analysis of particle image velocimetry data. *Exp. Fluids* **32** (1), 76–86.
- CAMUSSI, R. & DI FELICE, F. 2006 Statistical properties of vortical structures with spanwise vorticity in zero pressure gradient turbulent boundary layers. *Phys. Fluids* **18** (3), 035108.
- CAMUSSI, R., GRILLIAT, J., CAPUTI-GENARO, G. & JACOB, M.C. 2010 Experimental study of a tip leakage flow: wavelet analysis of pressure fluctuations. *J. Fluid Mech.* **660**, 87–113.
- CAMUSSI, R. & GUJ, G. 1997 Orthonormal wavelet decomposition of turbulent flows: intermittency and coherent structures. *J. Fluid Mech.* **348**, 177–199.
- CAMUSSI, R., ROBERT, G. & JACOB, M.C. 2008 Cross-wavelet analysis of wall pressure fluctuations beneath incompressible turbulent boundary layers. *J. Fluid Mech.* **617**, 11–30.
- CHEN, S. & CAO, N. 1997 Anomalous scaling and structure instability in three-dimensional passive scalar turbulence. *Phys. Rev. Lett.* **78** (18), 3459–3462.
- CHOWDHURI, S., IACOBELLO, G. & BANERJEE, T. 2021 Visibility network analysis of large-scale intermittency in convective surface layer turbulence. *J. Fluid Mech.* **925**, A38.
- CHOWDHURI, S., KUMAR, S. & BANERJEE, T. 2020 Revisiting the role of intermittent heat transport towards Reynolds stress anisotropy in convective turbulence. *J. Fluid Mech.* **899**, A26.
- CORKE, T., ARNDT, A., MATLIS, E. & SEMPER, M. 2018 Control of stationary cross-flow modes in a Mach 6 boundary layer using patterned roughness. *J. Fluid Mech.* **856**, 822–849.
- CORKE, T.C., SHAKIB, F. & NAGIB, H.M. 1991 Mode selection and resonant phase locking in unstable axisymmetric jets. *J. Fluid Mech.* **223** (1), 253–311.
- CRAIG, S.A., HUMBLE, R.A., HOFFERTH, J.W. & SARIC, W.S. 2019 Nonlinear behaviour of the Mack mode in a hypersonic boundary layer. *J. Fluid Mech.* **872**, 74–99.
- CRAWLEY, M., GEFEN, L., KUO, C.W., SAMIMY, M. & CAMUSSI, R. 2018 Vortex dynamics and sound emission in excited high-speed jets. *J. Fluid Mech.* **839**, 313–347.
- CUI, G. & JACOBI, I. 2021 Biphasic as a diagnostic for scale interactions in wall-bounded turbulence. *Phys. Rev. Fluids* **6** (1), 014604.
- CUI, Y., ZHANG, H. & ZHENG, X. 2024 Turbulence modulation by charged inertial particles in channel flow. *J. Fluid Mech.* **990**, A2.
- DAUBECHIES, I. 1992 *Ten Lectures On Wavelets*. Society for Industrial and Applied Mathematics.
- DI RENZO, M. & URZAY, J. 2018 Aerodynamic generation of electric fields in turbulence laden with charged inertial particles. *Nat. Commun.* **9** (1), 1676.
- DUDOK DE WIT, T. & KRASNOSEL'SKIKH, V.V. 1995 Wavelet bicoherence analysis of strong plasma turbulence at the earth's quasiparallel bow shock. *Phys. Plasmas* **2** (11), 4307–4311.
- EATON, J.K. & FESSLER, J. 1994 Preferential concentration of particles by turbulence. *Intl J. Multiphase Flow* **20**, 169–209.
- ELGAR, S. & GUZA, R.T. 1985 Observations of bispectra of shoaling surface gravity waves. *J. Fluid Mech.* **161**, 425–448.
- ELGHOBASHI, S. 1994 On predicting particle-laden turbulent flows. *Appl. Sci. Res.* **52** (4), 309–329.
- FARGE, M. 1992 Wavelet transforms and their applications to turbulence. *Annu. Rev. Fluid Mech.* **24** (1), 395–458.
- FARGE, M., PELLEGRINO, G. & SCHNEIDER, K. 2001 Coherent vortex extraction in 3D turbulent flows using orthogonal wavelets. *Phys. Rev. Lett.* **87** (5), 054501.
- FOKEN, T. & WICHURA, B. 1996 Tools for quality assessment of surface-based flux measurements. *Agric. Forest Meteorol.* **78** (1–2), 83–105.
- FRISCH, U. 1995 *Turbulence: The Legacy of A.N. Kolmogorov*. Cambridge University Press.

- GRASSUCCI, D., CAMUSSI, R., JORDAN, P. & GRIZZI, S. 2015 Intermittency of the near pressure field induced by a compressible coaxial jet. *Exp. Fluids* **56** (2), 23.
- GRINSTED, A., MOORE, J.C. & JEVREJEVA, S. 2004 Application of the cross wavelet transform and wavelet coherence to geophysical time series. *Nonlinear Process. Geophys.* **11** (5/6), 561–566.
- GROSSHANS, H., BISSINGER, C., CALERO, M. & PAPALEXANDRIS, M.V. 2021 The effect of electrostatic charges on particle-laden duct flows. *J. Fluid Mech.* **909**, A21.
- GROSSHANS, H. & PAPALEXANDRIS, M.V. 2017 Direct numerical simulation of triboelectric charging in particle-laden turbulent channel flows. *J. Fluid Mech.* **818**, 465–491.
- GUJ, G. & CAMUSSI, R. 1999 Statistical analysis of local turbulent energy fluctuations. *J. Fluid Mech.* **382**, 1–26.
- HASSELMANN, K., MUNK, W. & MACDONALD, G. 1963 Bispectra of ocean waves. In *Proceedings of the Symposium on Time Series Analysis* (ed. M. Rosenblatt), vol. 1, pp. 125–139. John Wiley
- HORWITZ, J.A.K. & MANI, A. 2020 Two-way coupled particle–turbulence interaction: effect of numerics and resolution on fluid and particle statistics. *Phys. Rev. Fluids* **5** (10), 104302.
- HUDGINS, L., FRIEHE, C.A. & MAYER, M.E. 1993 Wavelet transforms and atmospheric turbulence. *Phys. Rev. Lett.* **71** (20), 3279–3282.
- HUTCHINS, N., CHAUHAN, K., MARUSIC, I., MONTY, J. & KLEWICKI, J. 2012 Towards reconciling the large-scale structure of turbulent boundary layers in the atmosphere and laboratory. *Boundary-Layer Meteorol.* **145** (2), 273–306.
- HUTCHINS, N. & MARUSIC, I. 2007 Evidence of very long meandering features in the logarithmic region of turbulent boundary layers. *J. Fluid Mech.* **579**, 1–28.
- HWANG, Y., HUTCHINS, N. & MARUSIC, I. 2022 The logarithmic variance of streamwise velocity and k^{-1} conundrum in wall turbulence. *J. Fluid Mech.* **933**, A8.
- JANTAČ, S. & GROSSHANS, H. 2024 Suppression and control of bipolar powder charging by turbulence. *Phys. Rev. Lett.* **132** (5), 054004.
- KANAGY S.P.II & MANN, C.J. 1994 Electrical properties of eolian sand and silt. *Earth-Sci. Rev.* **36** (3–4), 181–204.
- KARNIK, A.U. & SHRIMPTON, J.S. 2012 Mitigation of preferential concentration of small inertial particles in stationary isotropic turbulence using electrical and gravitational body forces. *Phys. Fluids* **24** (7), 073301.
- KIM, B.H. & WILLIAMS, D.R. 2006 Nonlinear coupling of fluctuating drag and lift on cylinders undergoing forced oscillations. *J. Fluid Mech.* **559**, 335–353.
- KLEWICKI, J.C., PRIYADARSHANA, P.J.A. & METZGER, M.M. 2008 Statistical structure of the fluctuating wall pressure and its in-plane gradients at high Reynolds number. *J. Fluid Mech.* **609**, 195–220.
- KOLMOGOROV, A.N. 1941 The local structure of turbulence in incompressible viscous fluid for very large Reynolds number. *Dokl. Akad. Nauk SSSR* **30**, 299–303.
- KULICK, J.D., FESSLER, J.R. & EATON, J.K. 1994 Particle response and turbulence modification in fully developed channel flow. *J. Fluid Mech.* **277**, 109–134.
- KUNKEL, G.J. & MARUSIC, I. 2006 Study of the near-wall-turbulent region of the high-Reynolds-number boundary layer using an atmospheric flow. *J. Fluid Mech.* **548**, 375–402.
- LANCASTER, G., IATSENKO, D., PIDDE, A., TICCINELLI, V. & STEFANOVSKA, A. 2018 Surrogate data for hypothesis testing of physical systems. *Phys. Rep.* **748**, 1–60.
- LU, J., NORDSIEK, H., SAW, E.W. & SHAW, R.A. 2010 Clustering of charged inertial particles in turbulence. *Phys. Rev. Lett.* **104** (18), 184505.
- LU, J. & SHAW, R.A. 2015 Charged particle dynamics in turbulence: theory and direct numerical simulations. *Phys. Fluids* **27** (6), 065111.
- MARUSIC, I., MCKEON, B.J., MONKEWITZ, P.A., NAGIB, H.M., SMITS, A.J. & SREENIVASAN, K.R. 2010 Wall-bounded turbulent flows at high Reynolds numbers: recent advances and key issues. *Phys. Fluids* **22** (6), 065103.
- MARUSIC, I. & MONTY, J.P. 2019 Attached eddy model of wall turbulence. *Annu. Rev. Fluid Mech.* **51** (1), 49–74.
- MAXEY, M.R. 1987 The gravitational settling of aerosol particles in homogeneous turbulence and random flow fields. *J. Fluid Mech.* **174**, 441–465.
- MCCOMAS, C.H. & BRISCOE, M.G. 1980 Bispectra of internal waves. *J. Fluid Mech.* **97** (1), 205–213.
- MCGOWAN, H.A. & CLARK, A. 2008 A vertical profile of PM10 dust concentrations measured during a regional dust event identified by MODIS Terra, western Queensland, Australia. *J. Geophys. Res.-Earth Surf.* **113** (F2), F02S03.
- MENEVEAU, C. 1991 Analysis of turbulence in the orthonormal wavelet representation. *J. Fluid Mech.* **232** (1), 469–520.

- MIDDLEBROOKS, J.B., CORKE, T.C., MATLIS, E. & SEMPER, M. 2024 Cross-flow instability on a swept-fin cone at Mach 6: characteristics and control. *J. Fluid Mech.* **981**, A18.
- MIHANOVIĆ, H., ORLIĆ, M. & PASARIĆ, Z. 2009 Diurnal thermocline oscillations driven by tidal flow around an island in the Middle Adriatic. *J. Mar. Syst.* **78**, S157–S168.
- MONSALVE, E., BRUNET, M., GALLET, B. & CORTET, P.P. 2020 Quantitative experimental observation of weak inertial-wave turbulence. *Phys. Rev. Lett.* **125** (25), 254502.
- NARAYANAN, S. & HUSSAIN, F. 1996 Measurements of spatiotemporal dynamics in a forced plane mixing layer. *J. Fluid Mech.* **320**, 71–115.
- NICKELS, T.B., MARUSIC, I., HAFEZ, S. & CHONG, M.S. 2005 Evidence of the k_1^{-1} law in a high-Reynolds-number turbulent boundary layer. *Phys. Rev. Lett.* **95**, 074501.
- PAQUIN, L.A., HAMEED, A., PARZIALE, N.J. & LAURENCE, S.J. 2024 Time-resolved wave packet development in highly cooled hypersonic boundary layers. *J. Fluid Mech.* **983**, A36.
- PATERNA, E., CRIVELLI, P. & LEHNING, M. 2016 Decoupling of mass flux and turbulent wind fluctuations in drifting snow. *Geophys. Res. Lett.* **43** (9), 4441–4447.
- PERCIVAL, D.P. 1995 On estimation of the wavelet variance. *Biometrika* **82** (3), 619–631.
- PERRY, A.E., HENBEST, S. & CHONG 1986 A theoretical and experimental study of wall turbulence. *J. Fluid Mech.* **165** (1), 163–199.
- POPE, S.B. 2000 *Turbulent Flows*. Cambridge University Press.
- RAHMAN, M.M., CHENG, W. & SAMTANEY, R. 2021 Generation and sustenance of electric fields in sandstorms. *Phys. Rev. Res.* **3** (1), L012008.
- RITZ, C.P. & POWERS, E.J. 1986 Estimation of nonlinear transfer functions for fully developed turbulence. *Physica D* **20**, 320–334.
- RUAN, X., GORMAN, M.T. & NI, R. 2024 Effects of electrostatic interaction on clustering and collision of bidispersed inertial particles in homogeneous and isotropic turbulence. *J. Fluid Mech.* **980**, A29.
- RUDGE, W.A.D. 1913 Atmospheric electrification during South African dust storms. *Nature* **91** (2263), 31–32.
- RUPPERT-FELSOT, J., FARGE, M. & PETITJEANS, P. 2009 Wavelet tools to study intermittency: application to vortex bursting. *J. Fluid Mech.* **636**, 427–453.
- SALEM, C., MANGENEY, A., BALE, S.D. & VELTRI, P. 2009 Solar wind magnetohydrodynamics turbulence: anomalous scaling and role of intermittency. *Astrophys. J.* **702** (1), 537–553.
- SCHMIDT, D.S., SCHMIDT, R.A. & DENT, J.D. 1998 Electrostatic force on saltating sand. *J. Geophys. Res.* **103** (D8), 8997–9001.
- SCHULTE, J.A. 2016 Wavelet analysis for non-stationary, nonlinear time series. *Nonlinear Process. Geophys.* **23** (4), 257–267.
- SHAO, Y. 2008 *Physics and Modelling of Wind Erosion*. Springer.
- SHINBROT, T. & HERRMANN, H.J. 2008 Granular matter: static in motion. *Nature* **451** (7180), 773–774.
- STOW, C.D. 1969 Dust and sand storm electrification. *Weather* **24** (4), 134–144.
- SUTHERLAND, W. 1893 LII. The viscosity of gases and molecular force. *London Edinburgh Dublin Philos. Mag. J. Sci.* **36** (223), 507–531.
- TORRENCE, C. & COMPO, G.P. 1998 A practical guide to wavelet analysis. *Bull. Am. Meteorol. Soc.* **79** (1), 61–78.
- UNNIKRISHNAN, S. & GAITONDE, D.V. 2020 Linear, nonlinear and transitional regimes of second-mode instability. *J. Fluid Mech.* **905**, A25.
- VAN MILLIGEN, B.P., HIDALGO, C. & SANCHEZ, E. 1995 Nonlinear phenomena and intermittency in plasma turbulence. *Phys. Rev. Lett.* **74** (3), 395–398.
- VAN MILLIGEN, B.P., SANCHEZ, E., ESTRADA, T., HIDALGO, C., BRAÑAS, B., CARRERAS, B. & GARCÍA, L. 1995 Wavelet bicoherence: a new turbulence analysis tool. *Phys. Plasmas* **2** (8), 3017–3032.
- WANG, G. & ZHENG, X. 2016 Very large scale motions in the atmospheric surface layer: a field investigation. *J. Fluid Mech.* **802**, 464–489.
- WANG, G., ZHENG, X. & TAO, J. 2017 Very large scale motions and PM10 concentration in a high-re boundary layer. *Phys. Fluids* **29** (6), 061701.
- WARHAFT, Z. 2000 Passive scalars in turbulent flows. *Annu. Rev. Fluid Mech.* **32** (1), 203–240.
- WATANABE, T. & GOTOH, T. 2004 Statistics of a passive scalar in homogeneous turbulence. *New J. Phys.* **6**, 40–40.
- WILLIAMS, E., NATHOU, N., HICKS, E., PONTIKIS, C., RUSSELL, B., MILLER, M. & BARTHOLOMEW, M.J. 2009 The electrification of dust-lofting gust fronts ('haboobs') in the Sahel. *Atmos. Res.* **91** (2–4), 292–298.
- XIANG, N.B. & QU, Z.N. 2018 Evolutionary characteristics of the interplanetary magnetic field intensity. *Astron. J.* **156** (4), 152.

- XU, G.S., WAN, B.N., SONG, M. & LI, J. 2003 Direct measurement of poloidal long-wavelength $E \times B$ flows in the HT-7 tokamak. *Phys. Rev. Lett.* **91** (12), 125001.
- YOUSEFI, A., COSTA, P., PICANO, F. & BRANDT, L. 2023 On the role of inertia in channel flows of finite-size neutrally buoyant particles. *J. Fluid Mech.* **955**, A30.
- ZHANG, H. 2024 Structure and coupling characteristics of multiple fields in dust storms. *Acta Mech. Sin.* **40** (3), 123339.
- ZHANG, H., CUI, Y. & ZHENG, X. 2023 How electrostatic forces affect particle behaviour in turbulent channel flows. *J. Fluid Mech.* **967**, A8.
- ZHANG, H. & LIU, Y. 2023 Three distinct scales dominate the role of eolian electric fields in dust turbulent transport. *Phys. Fluids* **35** (10), 101704.
- ZHANG, H., TAN, X. & ZHENG, X. 2023 Multifield intermittency of dust storm turbulence in the atmospheric surface layer. *J. Fluid Mech.* **963**, A15.
- ZHANG, H. & ZHOU, Y.H. 2020 Reconstructing the electrical structure of dust storms from locally observed electric field data. *Nat. Commun.* **11** (1), 5072.
- ZHANG, H. & ZHOU, Y.H. 2023 Unveiling the spectrum of electrohydrodynamic turbulence in dust storms. *Nat. Commun.* **14** (1), 408.
- ZHENG, X. 2009 *Mechanics of Wind-Blown Sand Movements*. Springer Science & Business Media.
- ZHENG, X.J. 2013 Electrification of wind-blown sand: recent advances and key issues. *Eur. Phys. J. E* **36** (12), 138.
- ZHENG, X.J., HUANG, N. & ZHOU, Y.H. 2003 Laboratory measurement of electrification of wind-blown sands and simulation of its effect on sand saltation movement. *J. Geophys. Res.-Atmos.* **108** (D10), 4322.
- ZHOU, Y.H. 2021 *Wavelet Numerical Method and Its Applications in Nonlinear Problems*. Springer.